

# Ultrathin silicon solar microcells for semitransparent, mechanically flexible and microconcentrator module designs

JONGSEUNG YOON<sup>1,2,3\*</sup>, ALFRED J. BACA<sup>3,4\*</sup>, SANG-IL PARK<sup>1,2,3</sup>, PAULIUS ELVIKIS<sup>5</sup>, JOSEPH B. GEDDES III<sup>2</sup>, LANFANG LI<sup>1,4</sup>, RAK HWAN KIM<sup>1,2,3</sup>, JIANLIANG XIAO<sup>6</sup>, SHUODAO WANG<sup>6</sup>, TAE-HO KIM<sup>1,2,3</sup>, MICHAEL J. MOTALA<sup>3,4</sup>, BOK YEOP AHN<sup>1,3</sup>, ERIC B. DUOSS<sup>1,3</sup>, JENNIFER A. LEWIS<sup>1,3</sup>, RALPH G. NUZZO<sup>1,3,4</sup>, PLACID M. FERREIRA<sup>5</sup>, YONGGANG HUANG<sup>6,7</sup>, ANGUS ROCKETT<sup>1</sup> AND JOHN A. ROGERS<sup>1,2,3,4,5†</sup>

<sup>1</sup>Department of Materials Science and Engineering, University of Illinois at Urbana-Champaign, Illinois 61801, USA

<sup>2</sup>Beckman Institute for Advanced Science and Technology, University of Illinois at Urbana-Champaign, Illinois 61801, USA

<sup>3</sup>Frederick Seitz Materials Research Laboratory, University of Illinois at Urbana-Champaign, Illinois 61801, USA

<sup>4</sup>Department of Chemistry, University of Illinois at Urbana-Champaign, Illinois 61801, USA

<sup>5</sup>Department of Mechanical Science and Engineering, University of Illinois at Urbana-Champaign, Illinois 61801, USA

<sup>6</sup>Department of Mechanical Engineering, Northwestern University, Evanston, Illinois 60208, USA

<sup>7</sup>Department of Civil and Environmental Engineering, Northwestern University, Evanston, Illinois 60208, USA

\*These authors contributed equally to this work

†e-mail: jrogers@uiuc.edu

Published online: 5 October 2008; doi:10.1038/nmat2287

The high natural abundance of silicon, together with its excellent reliability and good efficiency in solar cells, suggest its continued use in production of solar energy, on massive scales, for the foreseeable future. Although organics, nanocrystals, nanowires and other new materials hold significant promise, many opportunities continue to exist for research into unconventional means of exploiting silicon in advanced photovoltaic systems. Here, we describe modules that use large-scale arrays of silicon solar microcells created from bulk wafers and integrated in diverse spatial layouts on foreign substrates by transfer printing. The resulting devices can offer useful features, including high degrees of mechanical flexibility, user-definable transparency and ultrathin-form-factor microconcentrator designs. Detailed studies of the processes for creating and manipulating such microcells, together with theoretical and experimental investigations of the electrical, mechanical and optical characteristics of several types of module that incorporate them, illuminate the key aspects.

Research in silicon photovoltaics represents a robust and diverse effort, with foci that seek to improve performance, cost and capabilities of these systems, ranging from structures for light trapping<sup>1–3</sup> to advanced doping techniques<sup>4–7</sup>, innovative spherical<sup>8–10</sup>, rectangular<sup>11–13</sup> and ultrathin<sup>14–16</sup> cell designs and advanced manufacturing techniques<sup>17,18</sup>. The results presented here contribute to this progress by introducing practical means to create and manipulate monocrystalline Si solar cells that are much thinner (down to ~100 nm, or limited only by junction depth) and smaller (down to a few micrometres) than those possible with other process technologies<sup>19–21</sup>. The small sizes of the cells and the room-temperature schemes for integrating them into modules enable the use of thin, lightweight flexible substrates for ease of transport and installation. The ability to define the spacings between cells in sparse arrays provides a route to modules with engineered levels of transparency, thereby creating opportunities for use in windows and other locations that benefit from this feature. Alternatively, such layouts of cells

can be combined with moulded micro-optic concentrators to increase the power output and provide an unusual appearance with some aesthetic appeal. Such design attributes, together with the thin geometries of the microcells ( $\mu$ -cells), are also advantageous because they can optimally balance optical absorption and carrier separation/collection efficiency with materials usage and purity requirements to reduce system cost. The following describes these aspects, beginning with the materials and integration strategies, and following with characteristics of the  $\mu$ -cells and various different modules that incorporate them.

Figure 1a schematically illustrates the steps for fabricating ultrathin, monocrystalline silicon solar  $\mu$ -cells along with methods for integrating them into interconnected modules (Fig. 1b). The process, which builds on our recent work in single-crystalline silicon for flexible electronics<sup>22–24</sup>, begins with delineation of the lateral dimensions of microbar ( $\mu$ -bar) structures on a Si(111) p-type, boron-doped, single-crystalline Czochralski wafer with a resistivity of 10–20  $\Omega$  cm, which we refer to as the source wafer,

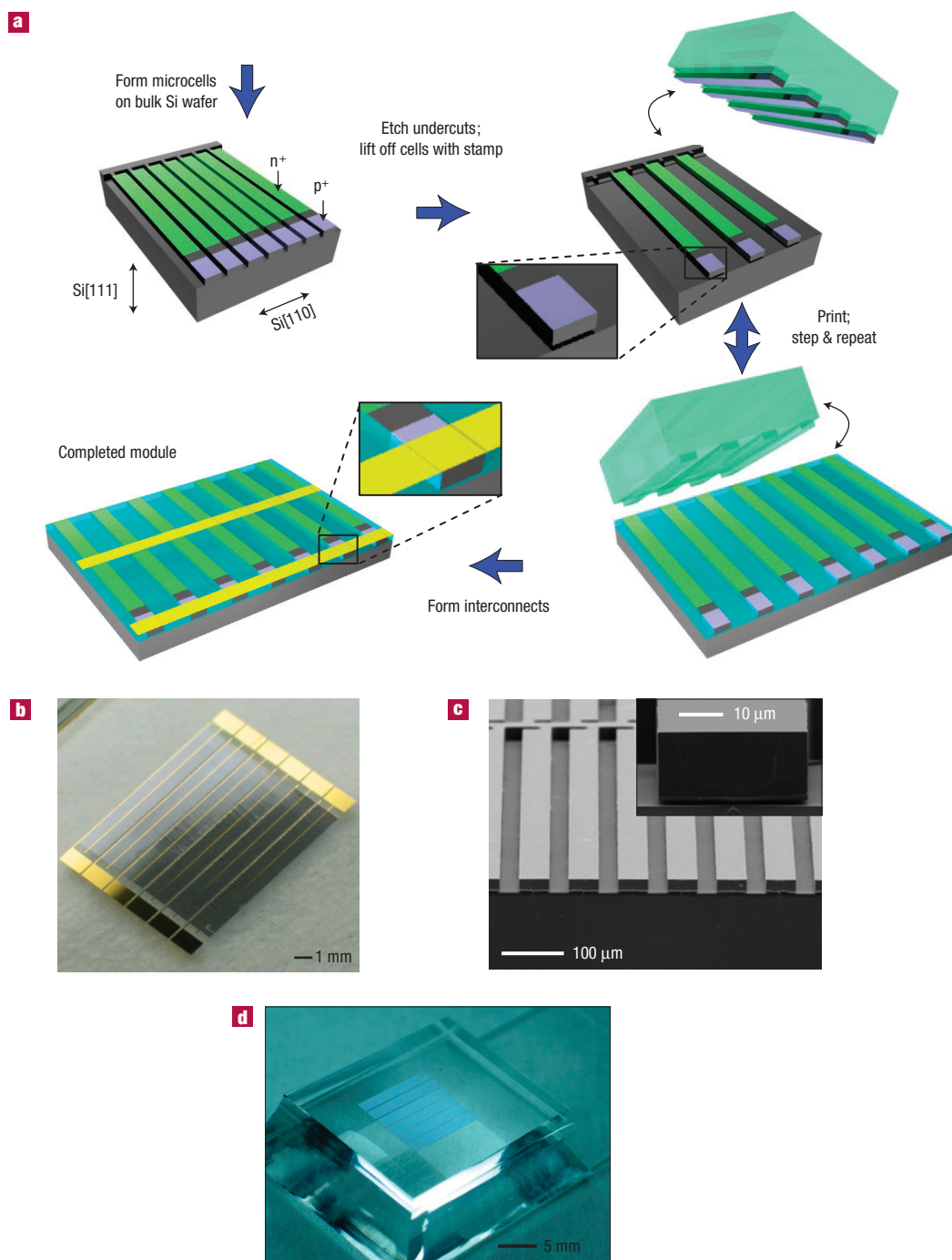


**Figure 1** Schematic illustrations, scanning electron microscopy (SEM) image and optical images of key steps in the fabrication of monocrystalline silicon photovoltaic modules that incorporate arrays of microscale solar cells ( $\mu$ -cells). **a**, Schematic illustration of steps for fabricating ultrathin  $\mu$ -cells from a bulk wafer, printing them onto a target substrate and forming electrical interconnections to complete a module. **b**, Optical image of a completed module consisting of printed  $\mu$ -cell arrays, interconnected by metal grid lines (Cr–Au, width  $\sim 80 \mu\text{m}$ , thickness  $\sim 0.6 \mu\text{m}$ ) that each connect 130  $\mu$ -cells. **c**, SEM image of an array of  $\mu$ -cells on a source wafer, ready for printing, after doping and KOH undercut. The inset shows a magnified cross-sectional SEM image of a typical  $\mu$ -cell, with thickness of  $\sim 20 \mu\text{m}$ . **d**, Optical image of an array of  $\mu$ -cells on a flat elastomeric poly(dimethylsiloxane) (PDMS) stamp, immediately after retrieval from a source wafer.

by etching through a patterned mask. Aligning the lengths of these structures perpendicular to the Si(110) direction of the wafer places their long axes along the preferential {110} etching plane for anisotropic, undercut etching with KOH. Regions of narrowed widths at the ends of the  $\mu$ -bars serve as anchors to retain

their lithographically defined positions throughout the processing. Maintaining sharp-angled corners at the positions of these anchors leads to stress focusing for controlled fracture<sup>25</sup> in the printing step, as described below. After etching, selective-area diffusion of boron ( $p^+$ ) and phosphorus ( $n^+$ ) from solid doping sources

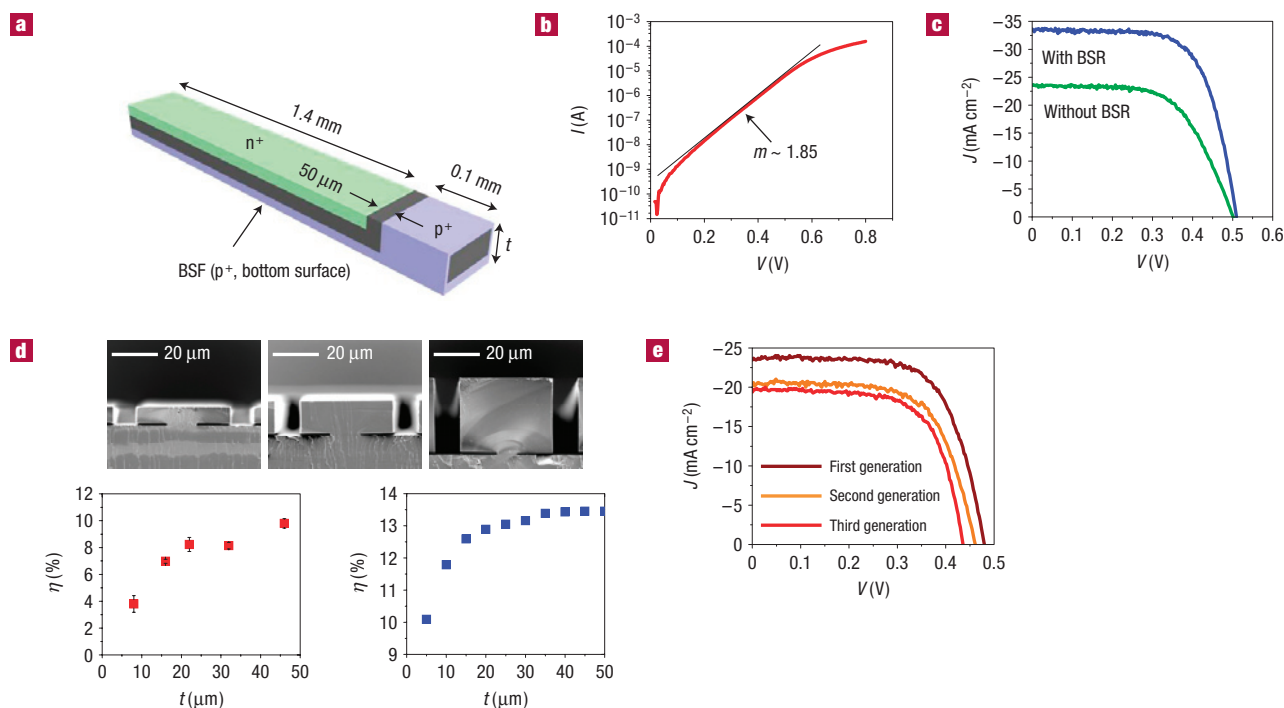


**Figure 2** Doping layout and performance characteristics of individual  $\mu$ -cells. **a**, Schematic illustration of a  $\mu$ -cell, showing the dimensions and the doping profiles. **b**, Semilog plot of the forward-bias dark-current ( $I$ )–voltage ( $V$ ) characteristics of an individual  $\mu$ -cell. The linear fit corresponds to a diode ideality factor ( $m$ ) of  $\sim 1.85$ . **c**, Representative current-density ( $J$ ) and voltage ( $V$ ) data from an individual  $\mu$ -cell with thickness of  $\sim 15 \mu\text{m}$  under Air Mass 1.5 (AM 1.5) illumination of  $1,000 \text{ W m}^{-2}$ , with and without a white diffuse backside reflector (BSR). **d**, SEM images, experimental efficiency ( $\eta$ ) data (with a metallic BSR) and PC-1D software modelling results corresponding to studies of the scaling properties with thicknesses between  $\sim 8$  and  $\sim 45 \mu\text{m}$ . **e**, Light  $J$ – $V$  curves of individual  $\mu$ -cells corresponding to the first, second and third generations from a single source wafer, with thickness of  $\sim 15 \mu\text{m}$ .

through patterned diffusion barriers of  $\text{SiO}_2$  creates rectifying pn junctions and top contacts. Deposition of etch masks ( $\text{SiO}_2$ – $\text{Si}_3\text{N}_4$ , Cr–Au) on the top surfaces and sidewalls of the  $\mu$ -bars followed by KOH etching releases them from the source wafer everywhere except at the positions of the anchors. Boron doping at the exposed bottom surfaces of the  $\mu$ -bars, again using a solid doping source, creates a back-surface field to yield fully functional Si solar  $\mu$ -cells. Figure 1c provides a scanning electron micrograph of a representative array of  $\mu$ -cells on a source wafer where the bars have lengths ( $L$ ), widths ( $W$ ) and thicknesses ( $t$ ) of 1.55 mm, 50  $\mu\text{m}$  and 15  $\mu\text{m}$ , respectively.

These  $\mu$ -cells can be selectively retrieved, by controlled fracture at the anchors, with a soft, elastomeric stamp (Fig. 1d) and then printed onto a substrate, in a room-temperature process with overall yields of  $\sim 99.9\%$  (ref. 26). Defining electrodes by an etch-back process after metal evaporation (Fig. 1b), by evaporation of metal through a shadow mask or by direct ink writing (see Supplementary Information, Fig. S1) interconnects the  $\mu$ -cells and completes the fabrication process. Figure 1b shows a module that incorporates 130  $\mu$ -cells on a glass substrate, where a photo-cured polymer (NOA61, Norland Products Inc.) serves as a planarizing layer and as an adhesive for the printing process. This device was fabricated with a flat stamp to create a system with  $\mu$ -cells in arrangements that match those on the source wafer. Stamps with appropriately designed relief features (see Supplementary Information, Figs S2–S3) can retrieve selected sets of  $\mu$ -cells and print them in layouts (for example spacings between adjacent  $\mu$ -cells) that are different from those on the source wafer<sup>27</sup>. For example, the  $\mu$ -cells can be printed in sparse arrays, using a

step-and-repeat process to enable overall module sizes that are much larger than that of the source wafer. These layouts enable semitransparent and micro-optic concentrator module designs, as described below. The source wafer can be reprocessed (following a surface re-polishing step using KOH etching, see Supplementary Information) after all of the  $\mu$ -cells are retrieved, to yield new generations of cells for additional rounds of printing. This process can be repeated until the entire wafer is consumed.

Figure 2a schematically illustrates the layout of a representative  $\mu$ -cell design, highlighting the details of the doping profiles. An individual cell ( $L = 1.55 \text{ mm}$ ) consists of phosphorus-doped ( $L_{n^+} = 1.4 \text{ mm}$ ), boron-doped ( $L_{p^+} = 0.1 \text{ mm}$ ) and un-doped ( $L_p = 0.05 \text{ mm}$ ) regions, respectively. The thicknesses,  $t$ , can be selected by suitable processing to lie between tens of micrometres and hundreds of nanometres. The boron-doped region on the top of the cell connects to the back-surface field on the bottom through doping on the sidewalls, in a manner that enables access to both emitter ( $n^+$ ) and base ( $p^+$ ) contacts on the top surface. This configuration greatly simplifies the process of electrical interconnection to form modules, by providing both contacts on the same side of the device. Surface doping concentrations of  $n^+$  (phosphorus),  $p^+$  (boron) and back-surface field (boron) regions are  $\sim 1.2 \times 10^{20} \text{ cm}^{-3}$ ,  $\sim 1.8 \times 10^{20} \text{ cm}^{-3}$  and  $\sim 5.8 \times 10^{19} \text{ cm}^{-3}$ , respectively, as measured by secondary-ion mass spectrometry<sup>28</sup> (see Supplementary Information). To fabricate interconnects with high yields, we identified two convenient means for planarizing the relief associated with the  $\mu$ -cells and for ensuring electrical isolation of the emitter and the base. The first uses a photocurable polymer as both an adhesive and planarization

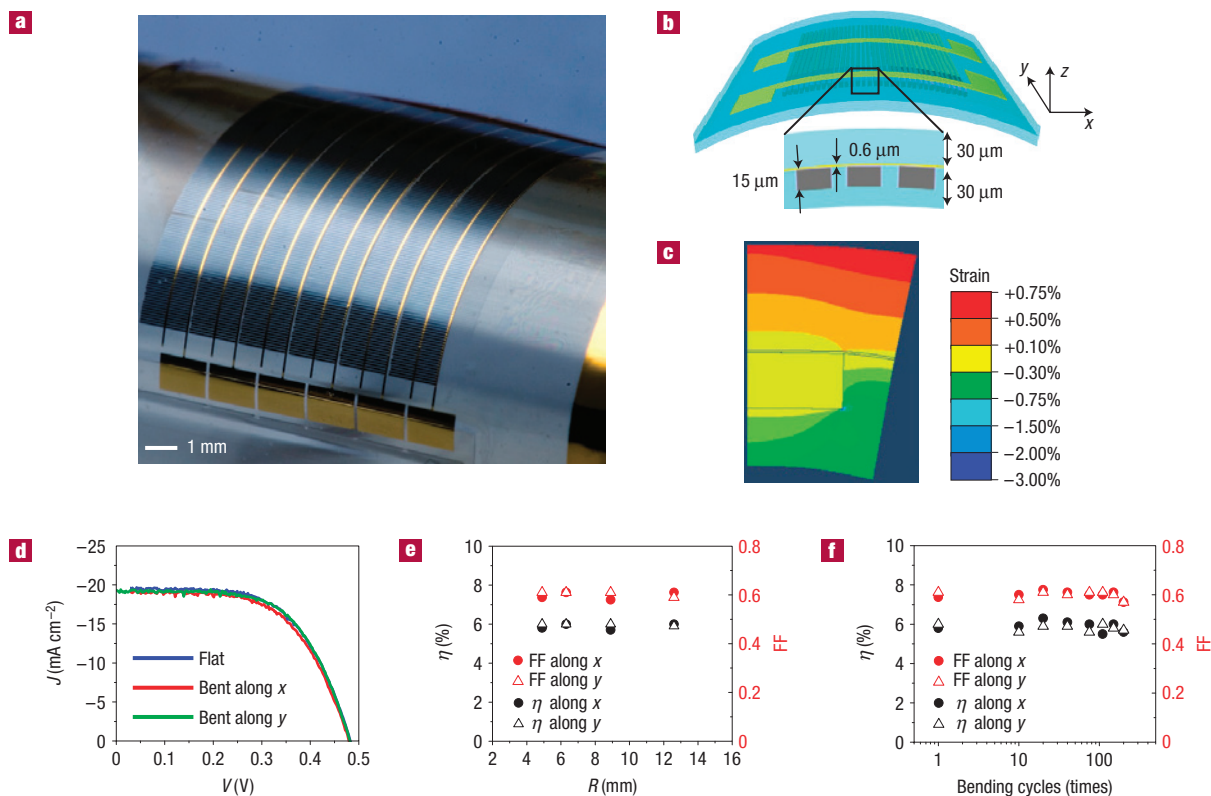


**Figure 3** Optical image, schematic illustration, mechanics modelling and photovoltaic performance of mechanically flexible modules that incorporate arrays of interconnected  $\mu$ -cells. **a**, Optical image of a module bent along a direction parallel to the widths of the  $\mu$ -cells, to a bending radius ( $R$ ) of 4.9 mm. **b**, Schematic illustration of an optimized design in which the neutral mechanical plane is positioned near the centre of the  $\mu$ -cells (grey) through judicious choices of thickness for the polymer (blue) substrate and overcoat. **c**, Colour contour plot of calculated bending strains ( $\epsilon_{xx}$ ) through the cross-section of a mechanically flexible  $\mu$ -cell module, bent along the cell width direction at  $R = 4.9$  mm. The calculations use symmetry boundary conditions for evaluation of a single unit cell of the system. The black lines delineate the boundaries of the  $\mu$ -cell and metal interconnect line (top). **d**,  $J-V$  data from a module under AM 1.5 illumination in a flat configuration and bent along the cell width ( $x$ ) and length ( $y$ ) directions, both for  $R = 4.9$  mm. **e**, Plot of  $\eta$  and fill factor (FF) under AM 1.5 illumination for  $R = 12.6, 8.9, 6.3$  and  $4.9$  mm. **f**, Plot of  $\eta$  and fill factor as a function of bending cycles up to 200 times at  $R = 4.9$  mm.

medium, as described in the context of Fig. 1 (see Supplementary Information, Fig. S4), such that a single step accomplishes both printing and planarization. Here, arrays of  $\mu$ -cells on the stamp press down into a liquid, photocurable polymer (NOA61) coated on the receiving substrate. The polymer fills the empty space between the  $\mu$ -cells by capillary action. Curing by ultraviolet exposure through the transparent stamp and then removing the stamp completes the process. The flat surface of the stamp coincides precisely with the top surfaces of the  $\mu$ -cells, to define the planarized surface of the module. Another approach (see Supplementary Information, Fig. S5), which is better suited to a step-and-repeat process, involves printing  $\mu$ -cells on a substrate that is coated with a layer ( $\sim 10 \mu\text{m}$  thick) of cured PDMS (Dow Corning) as a soft, elastomeric adhesive. Covering the printed  $\mu$ -cells with thin layers of  $\text{SiO}_2$  ( $\sim 150 \text{ nm}$  thick) and NOA61 ( $\sim 30 \mu\text{m}$  thick), pressing a flat piece of PDMS on top of the structure and then ultraviolet curing through the stamp accomplishes planarization with a tolerance (less than  $1 \mu\text{m}$ ) similar to that achieved in the first approach. In this second method, a short oxygen reactive-ion etching step is often needed to remove the thin, residual layer of NOA61 that tends to coat partially the top surfaces of the  $\mu$ -cells. In both approaches, the shallow junction depth ( $\sim 0.3 \mu\text{m}$ ) creates challenging demands on the extent of planarization. Extending the phosphorus doping down the sidewalls, to a distance of

$\sim 1/3$  of the  $\mu$ -cell thickness, as illustrated in Fig. 2a, relaxes the requirements on planarization. Direct ink writing and other approaches that form conformal electrodes provide further benefits in this sense.

$I-V$  measurements of individual  $\mu$ -cells and completed modules were made in the dark and in a simulated AM 1.5 illumination condition of  $1,000 \text{ W m}^{-2}$  at room temperature. Figure 2b shows a representative dark  $I-V$  curve recorded from an individual  $\mu$ -cell under forward bias, indicating a diode ideality factor ( $m$ ) of  $\sim 1.85$  at room temperature. Figure 2c shows  $I-V$  curves from typical  $\mu$ -cells with and without a backside reflector (BSR) under AM 1.5 illumination, evaluated without metal contacts or antireflection coatings. Without a BSR, this  $\mu$ -cell, which has  $t \sim 15 \mu\text{m}$ , shows a short-circuit current density,  $J_{sc}$ , of  $23.6 \text{ mA cm}^{-2}$ , an open-circuit voltage,  $V_{oc}$ , of 503 mV, a fill factor of 0.61 and an overall solar-energy conversion efficiency ( $\eta$ ) of 7.2%, where the calculations relied on the spatial dimensions of the  $\mu$ -cells rather than the surface area of the p-n junction. We also do not explicitly account for contributions from light incident on the edges of the cells. The device-to-device variations in properties of the  $\mu$ -cells of  $15\text{--}20 \mu\text{m}$  thickness without BSR are typically in the range of 6–8% (10–13% with BSR) for  $\eta$  and 450–510 mV for  $V_{oc}$ .

In this ultrathin regime, the absorption length of monocrystalline Si for near-infrared and visible wavelengths is

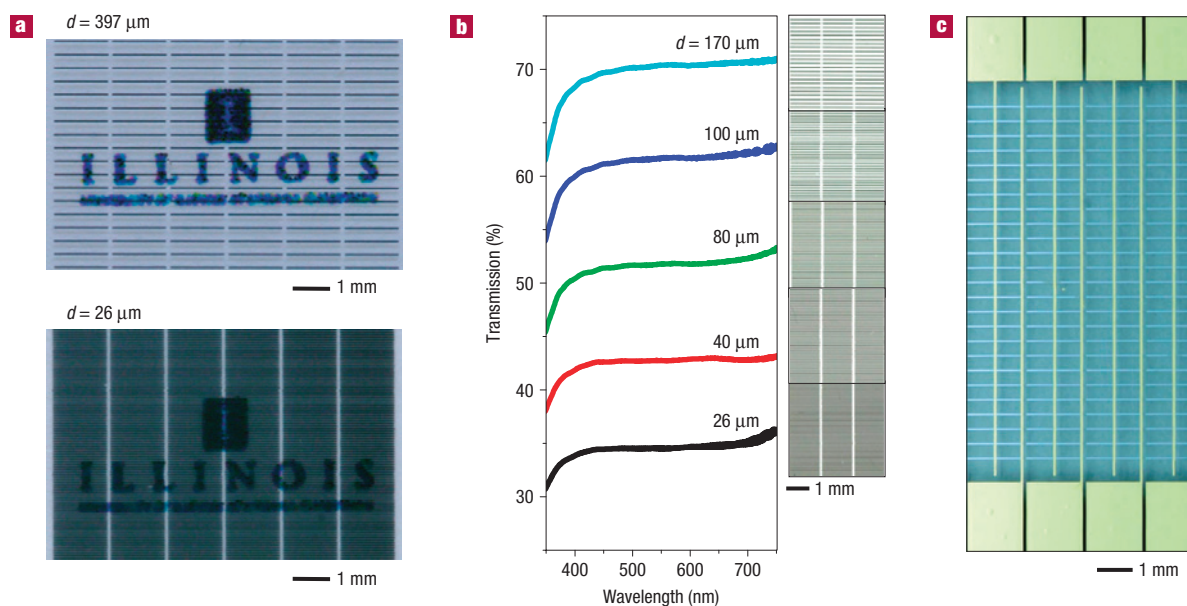


**Figure 4** Optical images and transmission spectra of printed, semitransparent  $\mu$ -cell arrays and interconnected modules. **a**, Optical images of printed  $\mu$ -cell arrays on PDMS- ( $\sim 10 \mu\text{m}$  thickness) coated polyethylene terephthalate substrates ( $\sim 50 \mu\text{m}$  thickness) at inter-cell spacings ( $d$ ) of  $26 \mu\text{m}$  and  $397 \mu\text{m}$ , respectively, resting on a piece of paper with text and logos to illustrate the differences in transparency. **b**, Transmission spectra recorded at normal incidence through printed semitransparent  $\mu$ -cell arrays with  $d = 26 \mu\text{m}$ ,  $40 \mu\text{m}$ ,  $80 \mu\text{m}$ ,  $100 \mu\text{m}$  and  $170 \mu\text{m}$ , respectively. Corresponding optical images of  $\mu$ -cell arrays are also shown. **c**, Optical image of an interconnected semitransparent module with  $d = 397 \mu\text{m}$ .

greater than or comparable to  $t$  (refs 29,30). As a result, the efficiency can be improved significantly by adding structures for light-trapping and/or a BSR. The top curve in Fig. 2c shows the effects of a diffuse white BSR, where  $J_{sc}$  and  $\eta$  increase to  $33.6 \text{ mA cm}^{-2}$  ( $\sim 42\%$  increase) and  $11.6\%$  ( $61\%$  increase), respectively. The  $J_{sc}$  value without a BSR in Fig. 2c is close to the theoretical maximum of  $\sim 26 \text{ mA cm}^{-2}$  that would be expected on the basis of the solar spectrum and absorption coefficient of Si, suggesting that the surface and contact recombination in the device was modest under short-circuit conditions. With the BSR the gain in  $J_{sc}$  to  $33.6 \text{ mA cm}^{-2}$  is consistent with a  $56 \mu\text{m}$  equivalent thickness (on the basis of the required thickness for sufficient absorption of light)<sup>29</sup>. The much higher optical path length shows that the BSR is working well.

To further examine the dependence of performance on thickness, we tested  $\mu$ -cells with  $t$  between  $\sim 8$  and  $\sim 45 \mu\text{m}$  and compared the measurements with numerical simulation of conventional cells using PC-1D software<sup>31</sup>, in vertical-type ( $n^+p-p^+$ ) configurations (see Supplementary Information, Fig. S6 and Table S1). Figure 2d shows the results, which indicate sharp increases in efficiency with thickness up to  $\sim 15 \mu\text{m}$ , followed by a gradual saturation from  $20$  to  $30 \mu\text{m}$  to a plateau above  $\sim 40 \mu\text{m}$ . Increases in efficiency with  $t$  are due mainly to increased absorption associated with the longer optical path lengths. For  $t$  above  $\sim 40 \mu\text{m}$ , however, the total absorption does not increase significantly, though the bulk recombination of minority carriers does. Although there are some quantitative differences between measurement and theory owing to non-ideal features of the  $\mu$ -cells (such as edge surface recombination due to un-passivated surfaces), the qualitative trends are consistent. These observations highlight the value of ultrathin (that is, less than  $40 \mu\text{m}$ ) cell designs, both in optimizing materials usage and in minimizing sensitivity to impurities that can lead to trapping of carriers. As described previously, multiple generations of such ultrathin

cells can be created from a single wafer. Figure 2e shows results from first-, second- and third-generation devices produced from a single source wafer in conventional vertical-type ( $n^+p-p^+$ ) cell configurations. Only moderate changes, comparable to typical cell-to-cell variations in properties, are observed. Improved doping profiles, ohmic contacts, antireflection coatings, surface texturization, light trapping structures, surface passivation layers and other advanced designs for monocrystalline Si cells can all be implemented within the schemes described here; each has the potential to provide improvements over the performance indicated in Fig. 2.

The  $\mu$ -cell designs and printing techniques enable new opportunities at the module level, with performance consistent with that of the individual cells. For example, the sequence in Fig. 1 separates high-temperature processing steps from the module substrate. As a result, integration of  $\mu$ -cells on rollable, plastic sheets, for ease of transport and installation, is possible. High levels of bendability can be achieved by exploiting optimized mechanical designs. The example shown in Fig. 3a,b involves a composite structure consisting of a planarizing/adhesive layer (NOA61; thickness  $\sim 30 \mu\text{m}$ ), which also serves as the substrate, arrays of  $\mu$ -cells and metal interconnects, and a polymer encapsulation layer (NOA61; thickness  $\sim 30 \mu\text{m}$ ). Spin-coating and then curing this encapsulation layer represents the final step in the fabrication sequence (see Supplementary Information, Fig. S7). Analytical modelling indicates that this module design places the neutral mechanical plane near the centre of the Si  $\mu$ -cells, such that the maximum strains in the silicon and metal interconnects (see Supplementary Information, Figs S8,S9), by far the most brittle materials in the system, are less than  $0.3\%$  even for bend radii less than  $5 \text{ mm}$ , for bending in any direction (that is, inward or outward, along the lengths of the  $\mu$ -cells or perpendicular to them) (see Supplementary Information, Figs S10,S11). Finite-element modelling, with representative results shown in Fig. 3c, confirms

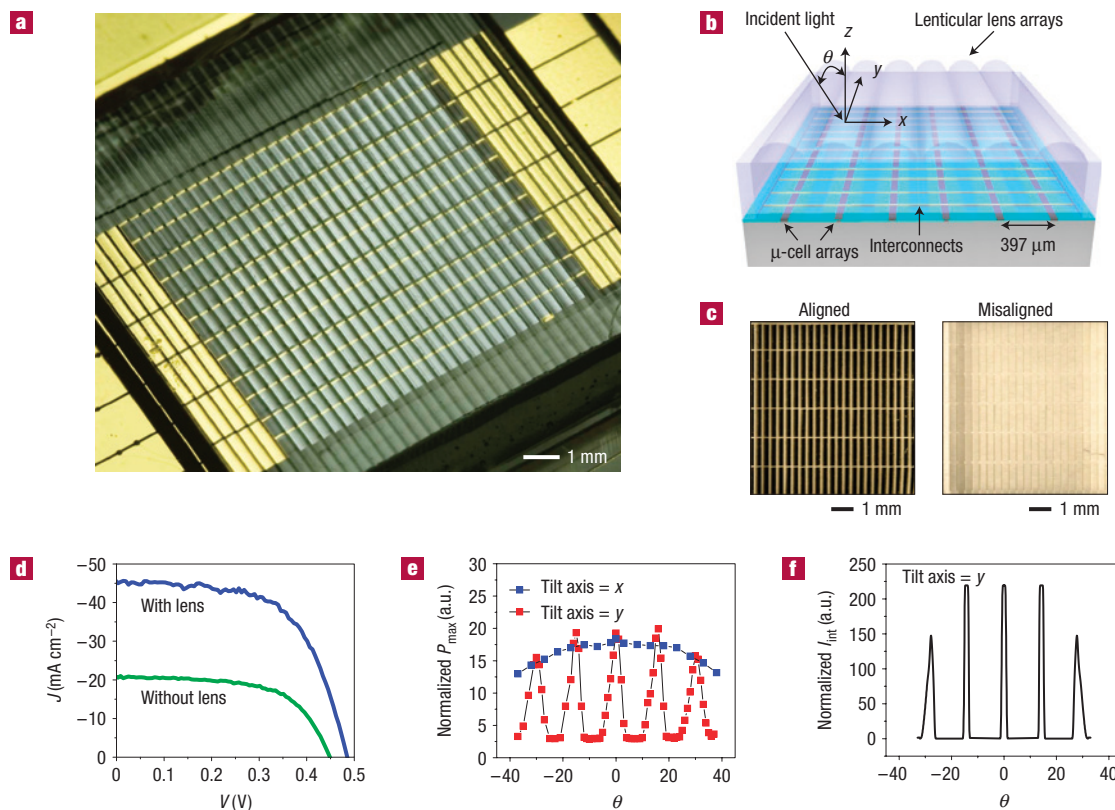


**Figure 5** Optical images, schematic illustration and performance characteristics of  $\mu$ -CPV modules. **a**, Optical image of a  $\mu$ -CPV module that combines moulded lenticular lens arrays and printed  $\mu$ -cells, viewed at an angle that corresponds to alignment of the focal positions of the lenses with the locations of the  $\mu$ -cells. **b**, Schematic illustration of this type of device. **c**, Optical images of lenticular lens arrays aligned (left) and misaligned (right) to arrays of printed  $\mu$ -cells, in the layout of the schematic illustration above. **d**,  $J$ - $V$  curves of this  $\mu$ -CPV module with and without the lenticular concentrator optics under AM 1.5 illumination. The lenses in these relatively low-concentration-ratio systems increase the current density and the maximum output power by  $\sim 2.5$  times. **e**, Normalized output power ( $P_{\text{out}}$ ) from a  $\mu$ -CPV module as a function of incidence angle ( $\theta$ ) for tilt along the  $x$  and  $y$  axes. Zero degrees corresponds to normal incidence. **f**, Normalized computed intensity ( $I_{\text{int}}$ ) integrated over the top surface of the  $\mu$ -cells as a function of  $\theta$  for tilting parallel to the cell length (with respect to the  $y$  axis). The periodicity observed results from focusing of light on  $\mu$ -cells from neighbouring sets of lenses.

these predictions (see Supplementary Information, Figs S12,S13). Module performance, evaluated in outward bending along and perpendicular to the cell length under AM 1.5 illumination, shows behaviour consistent with expectation on the basis of mechanics analysis and relative insensitivity of the degree of illumination across the modest area of the module, for the bend radii examined here. For example, at bending radii of 12.6, 8.9, 6.3 and 4.9 mm, the module efficiency ( $\sim 6.0\%$ ) and fill factor ( $\sim 0.60$ ) remain unchanged as summarized in Fig. 3d,e. Fatigue tests, with bending up to 200 cycles, also show little change in performance, as summarized in Fig. 3f. The slightly reduced module efficiency and fill factor compared with the individual cell performance can be partially attributed to the shadowing effect and resistive losses arising from metal interconnects.

Another feature of the module designs and fabrication processes introduced here is their ability to achieve definable levels of optical transparency, which can be valuable for applications in architectural or automotive glass and others. This outcome can be achieved either through the use of extremely thin  $\mu$ -cells (see, for example, Fig. 2d) or sparse arrays, defined by etching procedures or step-and-repeat printing. This latter approach is particularly easy to implement, and offers a significant degree of control over visually uniform levels of greyscale (that is, individual  $\mu$ -cells with dimensions reported here are not readily visible to the unaided eye).

Figure 4a shows printed text and logos viewed through arrays of  $\mu$ -cells with high and low areal coverages, to demonstrate the effect. Automated printers (see Supplementary Information, Fig. S14) enable programmable selection of coverages and, therefore, levels of transparency, for any given arrangement of  $\mu$ -cells on the source wafer. Figure 4b shows normal-incidence transmission spectra and optical micrographs for cases of cell spacings ranging from 170 to 26  $\mu\text{m}$  (areal coverages from 20% to 60%), corresponding to levels of transparency from  $\sim 70\%$  to  $\sim 35\%$ , all generated from arrays of  $\mu$ -cells on a single source substrate. The transmittance in each case is constant throughout the visible range, and increases approximately linearly with areal coverage, as expected. Figure 4c provides an image of a completed module, with interconnects, consisting of  $\mu$ -cells at a spacing of 397  $\mu\text{m}$ .

For cells in such layouts, concentrator photovoltaic designs that use integrated micro-optic focusing elements for ultrathin-form-factor microconcentrator photovoltaic ( $\mu$ -CPV) systems can improve the module's output power. Here, we demonstrate this possibility with moulded arrays of cylindrical lenses, for possible implementation with a single-axis tracker. These devices use arrays of  $\mu$ -cells with spacings ( $\sim 397 \mu\text{m}$ ) that match the layouts of low-cost, commercially available lenticular lens arrays (Edmund Optics), from which we could form replicas by soft lithographic moulding of a composite silicone-based epoxy

resin that was thermally matched to the photovoltaic module by filling with silica nanoparticles<sup>32</sup>. The radius of curvature of the commercial and replicated cylindrical microlenses was  $\sim 0.83$  mm, corresponding to a focal length of  $\sim 2.2$  mm. With collimated light, the widths of the focused lines of light (full-width at 90% maximum) were  $\sim 35$   $\mu\text{m}$ . We aligned the lens arrays to interconnected arrays of  $\mu$ -cells using a thin PDMS film as a spacer, and a coupler on an *XYZ* and angle-controlled stage. Figure 5a,b shows an optical image and a schematic illustration of such a  $\mu$ -CPV device. Figure 5c presents images corresponding to the cases when the lens arrays are aligned and misaligned to the  $\mu$ -cells. In the aligned state, the module seems to incorporate silicon at a nearly full areal coverage. When misaligned, the system assumes the colour of the module substrate, and the silicon is invisible. The *I*-*V* characteristics of a module with and without aligned lens arrays, under AM 1.5 illumination, are shown in Fig. 5d. The maximum output power with the lenses is  $\sim 2.5$  times larger than that without the lenses. This ratio is somewhat smaller than the expectation on the basis of simple estimates (see Supplementary Information), owing partly to the relatively large size of the light source in the solar simulator (91192-1000W, Oriel) and its close proximity to the module. These features result in a degree of collimation that is both non-ideal and substantially less than that of sunlight. However, the small area and ultrathin microdesigns presented here can in principle lead to consumption of less silicon material than conventional and related microspherical silicon concentrator modules<sup>9</sup>. Owing to the cylindrical geometry of the lenses and the bar shapes of the  $\mu$ -cells, decreases in output power associated with angular tilting about the *x*-axis are minimal, as illustrated in Fig. 5e. Rotations about the *y*-axis cause dramatic changes, consistent with the nature of the optics and the images shown in Fig. 5c. The periodicity observed in this case results from focusing of light on  $\mu$ -cells from neighbouring sets of lenses. The angular positions and relative values of the first, second and third peaks match well with simulated data from numerical ray-tracing calculations (Fig. 5f).

The types of module reported here may create new possibilities for monocrystalline silicon photovoltaics, particularly in applications that benefit from thin, lightweight construction, mechanical flexibility, semitransparency or the unusual optical properties of the  $\mu$ -CPV designs. In most cases, we chose materials that have the potential for long lifetime and high reliability. The procedures themselves are compatible with substrates, encapsulation, adhesive and optical materials used in existing photovoltaic systems. Similarly, as noted previously, advanced monocrystalline silicon cell designs and enhancement techniques can also be incorporated for improved performance. Although the focus of the strategies presented here is on module capabilities and designs, rather than cost or performance, a notable feature of these approaches is that the ultrathin cell geometries and, for  $\mu$ -CPV and semitransparent designs, the sparse coverages represent efficient ways to use silicon. The former aspect can also relax requirements on the purity of the silicon. An obvious consequence of these aspects is the potential to reduce the silicon component of the module cost. Such reductions are balanced, however, by increased processing costs associated with creating and interconnecting the  $\mu$ -cells. Low-cost printing, doping and etching techniques suitable for high-performance  $\mu$ -cell and module fabrication, together with other means to reduce cost or increase performance, are, therefore, important areas for further work.

## METHODS

### FABRICATING MICROCELLS

The fabrication process began with a p-type (111) Czochralski Si wafer (3 inch diameter, 10–20  $\Omega$  cm, 375  $\mu\text{m}$  thickness, Montco Silicon Technology) that

was coated with a layer of  $\text{SiO}_2$  ( $\sim 600$  nm) formed by plasma-enhanced chemical vapour deposition (PlasmaTherm SLR) at 250 °C. Spin casting, exposing (365 nm light, through a Karl Suss MJB mask aligner) and developing a layer of photoresist (AZ5214, Clariant; developer, AZ327MIF, Clariant) formed a pattern that defined the lateral dimensions and layouts of the  $\mu$ -cells, in rectangular geometries (that is,  $\mu$ -bars). The  $\text{SiO}_2$  not protected by the resist was removed with buffered oxide etchant (6:1, Transene). Inductively coupled plasma reactive-ion etching (STS)<sup>23,24</sup> formed trench structures with typical depths of 15–20  $\mu\text{m}$  in the regions of exposed silicon. The photoresist and remaining  $\text{SiO}_2$  were then removed with acetone and hydrofluoric acid (HF, Fisher, 49% concentration), respectively. Selective area doping of top contacts was conducted using solid-state sources of boron (BN-1250, Saint Gobain) and phosphorus (PH-1000N, Saint Gobain) at 1,000 °C under  $\text{N}_2$  atmosphere for 30 min (boron) and 10 min (phosphorus). A layer of  $\text{SiO}_2$  (900 nm) deposited by plasma-enhanced chemical vapour deposition at 250 °C and patterned by photolithography (photoresist, AZ4620, Clariant; developer, deionized  $\text{H}_2\text{O}:\text{AZ400K} = 3:1$  by volume, Clariant) and etching in buffered oxide etchant served as a doping mask. The doped wafer was then cleaned and coated with  $\text{SiO}_2$  (100 nm) and  $\text{Si}_3\text{N}_4$  (500 nm) by plasma-enhanced chemical vapour deposition at 250 °C, and subsequently with Cr (80 Å) and Au (800 Å) via directional deposition in an electron-beam evaporator (Temescal, FC 1800) at an angle of  $\pm 30^\circ$  with respect to the wafer surface. Reactive-ion etching (PlasmaTherm 790 series) using  $\text{CHF}_3\text{-O}_2$  (40–2 s.c.c.m., 50 mtorr, 150 W, 7 min) and  $\text{SF}_6$  (40 s.c.c.m., 50 mtorr, 100 W, 1 min) exposed regions of Si at the bottoms of the trenches formed by inductively coupled plasma reactive-ion etching. Immersion in KOH (PSE-200, Transene) at 100 °C for  $\sim 30$  min initiated anisotropic undercut etching at these locations to define the bottom surfaces of the  $\mu$ -cells with overall yields of over 99%. After removing Au and Cr with commercial etchants (Transene), these bottom surfaces were doped with boron again using the solid-state doping source at 1,000 °C for 5 min. Cleaning of the resulting sample in Piranha solution ( $\text{H}_2\text{SO}_4:\text{H}_2\text{O}_2 = 3:1$  by volume, 3 min) and HF completed the process.

### FABRICATING ELASTOMERIC STAMPS

Simple, flat stamps for by-hand printing were prepared by curing a PDMS prepolymer and cross-linking agent (Sylgard 184, Dow Corning Corp.) mixed at 10:1 by volume at 75 °C for 2 h. Forming composite stamps suitable for use in our automated printer system involved several steps (see Supplementary Information, Fig. S3). First, the template that defined the geometry of relief on the stamp was prepared on a Si wafer (4 inch diameter) by optical lithography using a negative-tone photoresist (SU8-50, 100  $\mu\text{m}$  thickness, Microchem) and a developer (SU-8 developer, Microchem). This substrate was then exposed to a vapour of (tridecafluoro-1,2,2-tetrahydrooctyl)-1-trichlorosilane (T2492-KG, United Chemical Technologies) for 3 h at room temperature. A 10:1 PDMS prepolymer mixture was poured onto the substrate, to a thickness of 100–200  $\mu\text{m}$ , and then partially cured at 75 °C for 30 min. A thin glass disc ( $\sim 0.1$  mm thickness, 3 inch diameter, Corning Incorporated) was placed on top, to form a backing layer capable of reducing in-plane deformations during printing. As a final step, another layer of 10:1 PDMS prepolymer mixture was poured on top. The entire composite stamp was heated at 75 °C for 2 h, to complete the curing.

### TRANSFER PRINTING MICROCELLS

Transfer printing used a custom-built, automated machine consisting of motion-controlled stages with 1  $\mu\text{m}$  resolution and an optical microscope vision system with a zoom range of  $4\times$  to  $26\times$ . Vacuum chucks mount on manually controlled rotational stages with 6 arc seconds sensitivity to support the processed wafers and the target substrates and to align them with each other and the relief features of the stamp. These chucks rest on a computer-controlled stage capable of 8 inches of motion in the *X* and *Y* directions. A PDMS composite stamp bolts into a vertical printhead assembly that can move in the vertical (*Z*) direction up to 2 inches. The stamp mount has a square, 3 inch aperture enabling an optical microscope vision system to image through the transparent composite stamp onto the stages below. The steps for printing are as follows.

To ensure high yields, it is critical that all components of the system are properly aligned. The tilt of the PDMS composite stamp relative to the source wafer and target substrate was manually adjusted, with 20 arc seconds of sensitivity, using the vision system for guidance. The  $\mu$ -cells on the source wafer were aligned to the corresponding relief features on the composite stamp using

rotational stages on the *XY* stage. A two-point calibration must be carried out on the source wafer, target substrate and cleaning substrate (six points in total) to account for tilt in the *Y* direction as well as misalignment of the *XY* motion axes relative to the orientation of the stamp.

Unlike alignment, the printing itself was fully automated. *XYZ* calibration data were first entered into custom software along with the desired spacing and number of rows in the printed cell arrays. This software calculated *XYZ* data for each pickup, print and cleaning position. The stages used these data to guide the printing process in a step-and-repeat procedure. The cycle time for a single pickup and printing procedure was approximately three minutes. One minute was required for positioning, pickup, printing and cleaning. For two minutes the cells were allowed to rest on the PDMS substrate before printing to increase adhesion.

#### PLANARIZING MICROCELLS

In planarization method 1, a precleaned substrate (glass or polyethylene terephthalate) was exposed to ultraviolet-induced ozone for 10 min and then spin-coated with an ultraviolet-curable polymer (NOA61, Norland Products Inc.). Retrieved  $\mu$ -cells on a flat PDMS stamp were placed against this substrate and then the entire system was exposed to an ultraviolet source for  $\sim 30$  min to cure the NOA. The PDMS stamp was then slowly peeled from the substrate, leaving planarized  $\mu$ -cells in a NOA matrix.

In planarization method 2, after printing arrays of  $\mu$ -cells on a substrate with a thin PDMS coating, SiO<sub>2</sub> (150 nm) was deposited by electron-beam evaporation (Temescal, FC 1800). Spin-coating a layer of NOA61 ( $\sim 30$   $\mu$ m) and then contacting a bare, flat PDMS element caused the NOA to flow to conform to and planarize the relief presented by the  $\mu$ -cells. Curing the NOA by exposure to ultraviolet light followed by removal of the stamp and, sometimes, a brief exposure of the substrate to an oxygen reactive-ion etch (10 s.c.c.m., 50 mtorr, 150 W, 2–3 min) completed the process.

#### FABRICATION OF MICROCONCENTRATORS

A commercially available cylindrical lens array (Edmund Optics NT43-028) served as a 'master' for the formation of replica lenses by soft lithography. The process began with cleaning of the master in soapy water under ultrasonic vibration for 20 min, followed by the same process with deionized water, and finally blowing the structure dry with compressed nitrogen. This cleaned lens master was then exposed to a vapour of (tridecafluoro-1,2,2-tetrahydrooctyl)-1-trichlorosilane (T2492-KG, United Chemical Technologies) for 1 h. A glass spacer of 1 mm thickness placed between the lens master and a glass backing plate prepared the system for casting and curing of a 10:1 mixture of PDMS prepolymer and curing agent (Sylgard 184, Dow Corning Corp.) at room temperature for 48 h. Peeling away yielded a PDMS mould on a glass backing plate. A separate, optically flat PDMS slab on a glass backing plate was prepared in a similar way, with a flat silicon wafer instead of the lens master. The photocurable polymeric material from which lens array replicas were made was prepared using commercially available 9–15 nm silica nanoparticles (IPA-ST, Nissan Chemicals, Ltd), a silicone-based epoxy resin (PCB 35-54B, Polysci) and a coupling agent (3-glycidyloxypropyl)trimethoxysilane (Sigma-Aldrich) according to published procedures<sup>32</sup>. After exposure to a vapour of (tridecafluoro-1,2,2-tetrahydrooctyl)-1-trichlorosilane for 1 h, the negative mould and the flat PDMS surface were assembled with a  $\sim 2.2$  mm spacer. The photocurable polymer prepared as above was poured into the cavity and cured under ultraviolet (9 mW cm<sup>-2</sup>) exposure for 10 min. Removing the flat PDMS and negative mould completed the fabrication of the replica lens array. The long-term stability and cost of the moulded lens arrays are expected to be reasonable for solar applications owing to enhanced thermal, optical and mechanical properties of the composite system and the inexpensive soft-lithography replication process.

#### ELECTRICAL AND OPTICAL MEASUREMENTS

Light and dark *I*–*V* measurements of  $\mu$ -cells were carried out at room temperature using a d.c. source meter (model 2400, Keithley) operated by LabVIEW5, and a 1,000 W full-spectrum solar simulator (model 91192, 4 × 4 inch source diameter,  $\pm 4^\circ$  collimation, Oriel) equipped with AM 0 and AM 1.5 direct filters. The input power of light from the solar simulator was measured with a power meter (model 70260, Newport) and a broadband detector (model 70268, Newport) at the point where the sample's top surface was placed. A typical *I*–*V* scan was conducted between  $-0.5$  V and  $+0.6$  V with a 2.2 mV increment (500 data points). *I*–*V* measurements of individual

$\mu$ -cells were made after transfer printing, with cells in an array format on a glass substrate. The reported efficiencies are based on the top surface area of the  $\mu$ -cell, without specifically accounting for sidewall coupling of light. For electrical characterization of the mechanically flexible  $\mu$ -cell arrays, the completed module was attached to the outer surfaces of glass test tubes with various radii. The centre of the module was aligned for normal-incidence illumination (see Supplementary Information, Fig. S15). Owing to the small sample size ( $\sim 5.1$  mm × 1.6 mm), the average flux of light into the module's active area in the flat state is only slightly larger ( $\sim 1.05$  times) than that even in the most highly bent state studied here (that is,  $R = 4.9$  mm). Light and dark *I*–*V* measurements at various bending geometries (that is, outward bending, along the cell length and the cell width) and bending radii were then made at room temperature. For fatigue tests, one bending cycle was defined such that the module was bent, relaxed to a flat state and bent again over the test tube. *I*–*V* measurements were conducted at bent states after a selected number of bending cycles. *I*–*V* measurements of the  $\mu$ -CPV module were made under the same experimental conditions as non-concentrated modules without an additional active cooling system, where the *I*–*V* characteristics were maintained as stable as the non-concentrated case throughout the entire measurement process (a few hours).

Optical transmission spectra of semitransparent  $\mu$ -cell modules were obtained at normal incidence of light using an ultraviolet–visible–near-infrared spectrophotometer (CARY 5G, Varian). Data collection was conducted with an aperture of  $\sim 5$  mm diameter in the wavelength range between 350 and 750 nm, where baseline corrections for 0% (no light) and 100% (air) transmission were made.

#### OPTICS SIMULATION

The calculation was carried out with a commercial ray-tracing package (Rayica 3.0, Optica Software). We assumed that the rays of light were incident at one angle and had a wavelength of 550 nm, that the lens array was infinite and that Fresnel reflections were negligible. The curved surface of the lens array was profiled experimentally and fitted to a parabola; the width of each lens was  $\sim 0.4$  mm and its centre thickness was  $\sim 2.2$  mm. The lens material was taken to be BK7 glass (for the purposes of this calculation). The lens array was positioned 0.1 mm from the top surface of the  $\mu$ -cells, whose width was 0.05 mm. The integrated top surface intensity is an imperfect predictor of the power incident and absorbed by the  $\mu$ -cells. However, the periodicity of the  $\mu$ -cell response with incident angle is captured.

Received 16 June 2008; accepted 1 September 2008; published 5 October 2008.

#### References

- Campbell, P. & Green, M. A. Light trapping properties of pyramidally textured surfaces. *J. Appl. Phys.* **62**, 243–249 (1987).
- Heine, C. & Morf, R. H. Submicrometer gratings for solar-energy applications. *Appl. Opt.* **34**, 2476–2482 (1995).
- Feng, N.-N. *et al.* Design of highly efficient light-trapping structures for thin-film crystalline silicon solar cells. *IEEE Trans. Electron Devices* **54**, 1926–1933 (2007).
- Wenham, S. R., Honsberg, C. B. & Green, M. A. Buried contact silicon solar cells. *Sol. Energy Mater. Sol. Cells* **34**, 101–110 (1994).
- Sinton, R. A., Kwark, Y., Gan, J. Y. & Swanson, R. M. 27.5-Percent silicon concentrator solar-cells. *IEEE Electron Devices Lett.* **7**, 567–569 (1986).
- Kerschaver, E. V. & Beaucarne, G. Back-contact solar cells: A Review. *Prog. Photovolt.* **14**, 107–123 (2006).
- Zhao, J. H., Wang, A. H. & Green, M. A. 24.5% efficiency silicon PERT cells on MCZ substrates and 24.7% efficiency PERL cells on FZ substrates. *Prog. Photovolt.* **7**, 471–474 (1999).
- Biancardo, M. *et al.* Characterization of microspherical semi-transparent solar cells and modules. *Sol. Energy* **81**, 711–716 (2007).
- Liu, Z. X. *et al.* A concentrator module of spherical Si solar cell. *Sol. Energy Mater. Sol. Cells* **91**, 1805–1810 (2007).
- Minemoto, T. & Takakura, H. Fabrication of spherical silicon crystals by dropping method and their application to solar cells. *Jpn. J. Appl. Phys.* **46**, 4016–4020 (2007).
- Taguchi, M. *et al.* HIT (TM) cells—high-efficiency crystalline Si cells with novel structure. *Prog. Photovolt.* **8**, 503–513 (2000).
- Weber, K. J. *et al.* A novel low-cost, high-efficiency micromachined silicon solar cell. *IEEE Electron Devices Lett.* **25**, 37–39 (2004).
- Verlinden, P. J. *et al.* Sliver (R) solar cells: A new thin-crystalline silicon photovoltaic technology. *Sol. Energy Mater. Sol. Cells* **90**, 3422–3430 (2006).
- Brendel, R., Bergmann, R. B., Lolgen, P., Wolf, M. & Werner, J. H. Ultrathin crystalline silicon solar cells on glass substrates. *Appl. Phys. Lett.* **70**, 390–392 (1997).
- Brendel, R. Review of layer transfer processes for crystalline thin-film silicon solar cells. *Jpn. J. Appl. Phys.* **40**, 4431–4439 (2001).
- Tayanaka, H., Yamauchi, K. & Matsushita, T. Thin-film crystalline silicon solar cells obtained by separation of a porous silicon sacrificial layer. *Proc. 2nd World Conf. Photovolt. Sol. Energy Conv.* 1272–1275 (Institute of Electrical and Electronics Engineers (IEEE), 1998).
- Yamamoto, K. *et al.* Thin-film poly-Si solar cells on glass substrate fabricated at low temperature. *Appl. Phys. A* **69**, 179–185 (1999).
- Shah, A. *et al.* *Photovoltaic Specialists Conference, Conference Record of the Twenty-Sixth IEEE* 569–574 (Institute of Electrical and Electronics Engineers (IEEE), 1997).

19. Bergmann, R. B. Crystalline Si thin-film solar cells: A review. *Appl. Phys. A* **69**, 187–194 (1999).
20. Green, M. A. Crystalline and thin-film silicon solar cells: State of the art and future potential. *Sol. Energy* **74**, 181–192 (2003).
21. Kazmerski, L. L. Solar photovoltaics R&D at the tipping point: A 2005 technology overview. *J. Electron Spectrosc. Relat. Phenom.* **150**, 105–135 (2006).
22. Mack, S., Meitl, M. A., Baca, A. J., Zhu, Z. T. & Rogers, J. A. Mechanically flexible thin-film transistors that use ultrathin ribbons of silicon derived from bulk wafers. *Appl. Phys. Lett.* **88**, 213101 (2006).
23. Ko, H. C., Baca, A. J. & Rogers, J. A. Bulk quantities of single-crystal silicon micro-/nanoribbons generated from bulk wafers. *Nano Lett.* **6**, 2318–2324 (2006).
24. Baca, A. J. *et al.* Printable single-crystal silicon micro/nanoscale ribbons, platelets and bars generated from bulk wafers. *Adv. Funct. Mater.* **17**, 3051–3062 (2007).
25. Meitl, M. A. *et al.* Stress focusing for controlled fracture in microelectromechanical systems. *Appl. Phys. Lett.* **90**, 083110 (2007).
26. Meitl, M. A. *et al.* Transfer printing by kinetic control of adhesion to an elastomeric stamp. *Nature Mater.* **5**, 33–38 (2006).
27. Lee, K. J. *et al.* Large-area, selective transfer of microstructured silicon: A printing-based approach to high-performance thin-film transistors supported on flexible substrates. *Adv. Mater.* **17**, 2332–2336 (2005).
28. Wilson, R. G., Stevie, F. A. & Magee, C. W. *Secondary Ion Mass Spectrometry: A Practical Handbook for Depth Profiling and Bulk Impurity Analysis* (Wiley, 1989).
29. Hull, R. (ed.) *Properties of Crystalline Silicon* (The Institution of Electrical Engineers (IEE), 1999).
30. Budianu, E., Purica, M., Rusu, E., Manea, E. & Gavrilă, R. *Semiconductor Conf. 2002. CAS 2002 Proc. Int. Vol. 1* (Institute of Electrical and Electronics Engineers (IEEE), 2002).
31. Clugston, D. A. & Basore, P. A. *Photovoltaic Specialists Conf. 1997., Conf. Record of the Twenty-Sixth IEEE 207–210* (Institute of Electrical and Electronics Engineers (IEEE), 1997).
32. Kunnavakkam, M. V. *et al.* Low-cost, low-loss microlens arrays fabricated by soft-lithography replication process. *Appl. Phys. Lett.* **82**, 1152–1154 (2003).

Supplementary Information accompanies the paper at [www.nature.com/naturematerials](http://www.nature.com/naturematerials).

### Acknowledgements

We thank T. Banks, K. Colravy and D. Sievers for help with processing, T. Spila for assistance with secondary-ion mass spectrometry measurements and H. Kim and D. Stevenson for help with photography. The materials parts of this effort were supported by the US Department of Energy (DoE), Division of Materials Sciences, under award DE-FG02-07ER46471, through the Materials Research Laboratory (MRL). The general characterization facilities were provided through the MRL with support from the University of Illinois and from DoE grants DE-FG02-07ER46453 and DE-FG02-07ER46471. The mechanics theory and the transfer-printing systems were developed under support from the Center for Nanoscale Chemical Electrical Mechanical Manufacturing Systems at the University of Illinois (funded by the NSF under grant DMI-0328162). J.Y. and J.B.G. acknowledge support from a Beckman postdoctoral fellowship. A.J.B. acknowledges support from the Department of Defense Science, Mathematics and Research for Transformation (SMART) fellowship.

### Author contributions

J.Y., J.A.L., R.G.N., P.M.F., Y.H., A.R. and J.A.R. designed the experiments. J.Y., A.J.B., S.-I.P., P.E., L.L., R.H.K., T.-H.K., M.J.M., B.Y.A., E.B.D., J.A.L., R.G.N., P.M.F., Y.H., A.R. and J.A.R. carried out experiments. J.Y., A.J.B., S.-I.P., J.A.L., R.G.N., P.M.F., Y.H., A.R. and J.A.R. analysed the data. P.E., J.Y., R.H.K., T.-H.K., J.A.L., R.G.N., P.M.F., Y.H., A.R. and J.A.R. contributed to transfer printing. J.X., S.W., Y.H., J.A.L., R.G.N., P.M.F., Y.H., A.R. and J.A.R. contributed to mechanics modelling and analysis. J.B.G., J.A.L., R.G.N., P.M.F., Y.H., A.R. and J.A.R. contributed to optics simulation. J.Y., A.J.B., J.A.L., R.G.N., P.M.F., Y.H., A.R. and J.A.R. wrote the paper.

### Author information

Reprints and permissions information is available online at <http://npg.nature.com/reprintsandpermissions>. Correspondence and requests for materials should be addressed to J.A.R.

## SUPPLEMENATRY METHODS

### Surface re-polishing of source wafer for multiple generation device fabrication

After all of the  $\mu$ -cells were retrieved, chemical re-polishing of the source wafer was conducted in KOH (PSE-200, Transene) at 120 °C for ~45 min to remove the relief features associated with the anchors and any residual doped areas. The processed source wafer has a root mean square (RMS) roughness of ~11 nm (over the area of 30  $\mu$ m by 15  $\mu$ m) as measured by atomic force microscopy (AFM). The re-polished source wafer was then cleaned by RCA cleaning methods<sup>1,2</sup> before additional rounds of  $\mu$ -cell fabrication.

1. Kern, W. Handbook of semiconductor wafer cleaning technology: Science, technology, and applications (Noyes Publications, Park Ridge, N.J., U.S.A, 1993).
2. Kern, W. Hydrogen peroxide solutions for silicon wafer cleaning. *RCA Eng* **28**, 99-105 (1983).

### Secondary ion mass spectrometry (SIMS)

Dynamic secondary ion mass spectrometry (SIMS) experiments were performed on a Cameca ims 5f instrument. Boron depth profiles were obtained using a 12 kV O<sub>2</sub><sup>+</sup> beam with a current of 100 nA, which was rastered over a 250  $\mu$ m square, and positive secondary ions were collected. Phosphorus depth profiles used a 10 kV Cs<sup>+</sup> beam with a current of 10 nA, which was rastered over a 150  $\mu$ m square, and negative secondary ions were collected. In all cases, secondary ions were collected on an electron multiplier. Ion implanted standards were used to determine relative sensitivity factors for each analyzed element in order to derive quantified results.

### Fabricating mechanically flexible $\mu$ -cell arrays

With a pre-cleaned and thin ( $\sim 50 \mu\text{m}$  thickness) film of polyethylene terephthalate (PET, Grafix DURA-LAR) as a handling substrate,  $\mu$ -cell arrays were printed and planarized onto an uncured NOA61 layer ( $\sim 30 \mu\text{m}$ ) using a flat PDMS stamp, as described in Figure S4. After the formation of metal interconnects (Cr/Au:  $\sim 0.6 \mu\text{m}$ ) using vacuum deposition and etch-back processes, a top layer of NOA61 ( $\sim 30 \mu\text{m}$ ) was added by spin-coating to implement a neutral mechanical plane. The fabrication step was completed by peeling off the PET substrate from the composite structure after full curing of the top NOA61 layer. Figure S7 depicts schematic illustrations of fabrication steps described above.

## SUPPLEMENATRY NOTE

### Analytical modeling of mechanically flexible $\mu$ -cell module: a position of neutral mechanical plane and strain in bending along the cell length direction

The mechanically flexible  $\mu$ -cell module is modeled as a composite beam as shown in Figure S8, where  $W$ ,  $W_{Si}$  and  $W_{NOA}$  are the widths of the beam, silicon  $\mu$ -cell and the distance between adjacent  $\mu$ -cells, respectively, and  $t$ ,  $t_m$ ,  $b$  and  $a-t$  are the thicknesses of the  $\mu$ -cell, metal interconnect layer, and NOA layers above and below the  $\mu$ -cell. The Young's modulus of silicon, metal (Au), and NOA are denoted by  $E_{Si}$ ,  $E_{Au}$  and  $E_{NOA}$ , respectively. The strain in the beam is given by  $\varepsilon_{yy} = (z - z_0)/R$ , where  $R$  is the bending

radius of the beam and  $z_0$  is the position of the neutral mechanical plane. In the case of without metal layer (i.e. Fig. S8(a)),  $z_0$  is given by

$$z_0 = \frac{a-t}{2} \frac{\left(1 + \frac{b}{a-t}\right)^2 + 2 \frac{b}{a-t} \frac{t}{a-t} + \frac{W_{NOA}}{W} \frac{t}{a-t} \left(2 + \frac{t}{a-t}\right) + \frac{E_{Si}t}{E_{NOA}(a-t)} \frac{W_{Si}}{W} \left(2 + \frac{t}{a-t}\right)}{1 + \frac{b}{a-t} + \frac{W_{NOA}}{W} \frac{t}{a-t} + \frac{E_{Si}t}{E_{NOA}(a-t)} \frac{W_{Si}}{W}}$$

, and is shown by the blue line in Figure S9. In the case of with metal layer (i.e. Fig. S8(b)),  $z_0$  is given by

$$z_0 = \frac{a-t}{2} \frac{\left(1 + \frac{b}{a-t}\right)^2 + 2 \frac{b}{a-t} \frac{t+t_m}{a-t} + \frac{W_{NOA}}{W} \frac{t}{a-t} \left(2 + \frac{t}{a-t}\right) + \frac{E_{Si}t}{E_{NOA}(a-t)} \frac{W_{Si}}{W} \left(2 + \frac{t}{a-t}\right) + \frac{E_{Au}t_m}{E_{NOA}(a-t)} \left(2 + \frac{2t+t_m}{a-t}\right)}{1 + \frac{b}{a-t} + \frac{W_{NOA}}{W} \frac{t}{a-t} + \frac{E_{Si}t}{E_{NOA}(a-t)} \frac{W_{Si}}{W} + \frac{E_{Au}t_m}{E_{NOA}(a-t)}}$$

, and is shown by the red line in Figure S9. Figure S11 depicts the strain ( $\epsilon_{yy}$ ) at the top and bottom surface of silicon  $\mu$ -cell with  $R = 4.9$  mm using analytical expressions described above.

### Finite element modeling of mechanically flexible $\mu$ -cell module: strain in bending along the cell width direction

The finite element method (FEM) is used to calculate strain of silicon  $\mu$ -cell module in bending along the cell width direction, as shown in Figure S12 and S13, with  $R = 4.9$  mm. The maximum strain in silicon for the inward and outward bending (with or without metal) is around 0.03%. The maximum strain in the metal layer is around 0.13% and is located at the silicon corner for both inward and outward bending as shown in Figure S14.

### Estimation of concentration ratio of lenticular lens

A simple estimation of concentration ratio of lenticular lens was made based on  $\mu$ -cell and lens dimensions, and measured intensity profile of lens as follows.

Assumptions:

1. The focal plane of the lens is located at the top surface of  $\mu$ -cells.
2. There is no optical loss due to the absorption of lens materials.
3. Optical losses from lens are caused by:
  - (a) reflection at the top and bottom surface of the lens:  $\sim 10\%$  ( $5\% \times 2$ ).
  - (b) The portion of the focused light outside the cell area, as determined from the measured intensity profile of the lens at focal plane:  $\sim 18\%$

The areal ratio of lens ( $A_L$ ) and  $\mu$ -cell ( $A_0$ ) is:  $A_L/A_0 = 397 \text{ mm}/50 \text{ mm} = \sim 7.9$ .

Loss factor (LF) due to (a) and (b) is:  $0.9 \times 0.82 = \sim 0.74$ .

Let the input intensity of incident light onto the lens surface  $I_0$ .

Then, the input power of light to the lens surface ( $A_L$ ) is:  $I_0 \times A_L = \sim 7.9I_0A_0$ .

The input power at the cell surface located at the focal plane of lens:  $LF \times 7.9I_0A_0 = \sim 5.9I_0A_0$ .

The concentration ratio is then estimated by

(Input power of light to cell surface with lens)/(Input power of light to cell surface without lens)

$= \sim 5.9I_0A_0/I_0A_0 = 5.9$ .

## SUPPLEMENATRY FIGURES

### FIGURE LEGENDS

**Figure S1:** (a) TEM micrograph of silver nanoparticles, withdrawn from an ink designed for direct writing of silver electrodes on silicon  $\mu$ -cells. Inset: Optical image of the concentrated silver ink (silver content = 65 wt%). (b) *IV* characteristics of silver electrodes (length = 1100  $\mu\text{m}$ , width = 15  $\mu\text{m}$ , height = 7  $\mu\text{m}$ ) printed by direct ink writing and cured for 3 h at constant temperature in air. The measured resistivities of the electrodes are: 1100  $\Omega\cdot\text{cm}$  at 150  $^{\circ}\text{C}$ ,  $1.76 \times 10^{-3}$   $\Omega\cdot\text{cm}$  at 175  $^{\circ}\text{C}$ ,  $2.2 \times 10^{-4}$   $\Omega\cdot\text{cm}$  at 200  $^{\circ}\text{C}$  and  $2.1 \times 10^{-5}$   $\Omega\cdot\text{cm}$  at 250  $^{\circ}\text{C}$ . (c) Optical image of silicon  $\mu$ -cell arrays interconnected with silver electrodes printed by direct writing of the silver nanoparticle ink. (d) SEM micrograph of silicon  $\mu$ -cells interconnected with silver electrodes. Inset: High magnification SEM image of the electrode (width:  $\sim 50$   $\mu\text{m}$ , height:  $\sim 20$   $\mu\text{m}$ ). (e) Optical image captured during direct ink writing of silver electrodes on a sparse array of silicon  $\mu$ -cells.

**Figure S2:** Schematic illustration of fabrication steps for a composite stamp having relief features, which is implemented for retrieving and printing selected sets of  $\mu$ -cells in automated printing process.

**Figure S3:** (a) Schematic illustration and (b) optical image of a completed composite stamp, which is designed to pick up and print 6  $\mu$ -cells simultaneously using an automated printing machine.

**Figure S4:** Schematic illustration of processing steps for printing and planarizing silicon  $\mu$ -cells at a single step using a flat PDMS stamp, where a photocurable polymer (NOA61,  $\sim 30 \mu\text{m}$ ) is used as both an adhesive and a planarizing medium. In this approach, the cell layout of printed  $\mu$ -cells is maintained as same as that of the source wafer.

**Figure S5:** Schematic illustration of processing steps for planarizing printed silicon  $\mu$ -cells, where  $\mu$ -cells were printed at selected cell spacings on a PDMS coated ( $\sim 10 \mu\text{m}$ ) substrate (glass or PET) through automated printing process.

**Figure S6:** Schematic illustration of silicon solar cell layout having  $n^+$ - $p$ - $p^+$  configuration, which is employed for calculating thickness dependence of cell efficiency using PC-1D<sup>®</sup>.

**Figure S7:** Schematic illustration of fabrication steps for mechanically flexible  $\mu$ -cell module, with key dimensions.

**Figure S8:** Cross-sectional schematic illustration of a model composite structure composed of silicon  $\mu$ -cell, and polymer encapsulation layer (a) without and (b) with metal layer, with key parameters.

**Figure S9:** Analytically calculated position ( $z_0$ ) of neutral mechanical plane as a function of the top polymer layer thickness ( $b$ ), where  $E_{Si} = 150 \text{ GPa}$ ,  $E_{NOA} = 1 \text{ GPa}$ ,  $E_{Au} = 78 \text{ GPa}$ ,  $a = 30 \mu\text{m}$ ,  $t = 15 \mu\text{m}$ ,  $t_m = 0.6 \mu\text{m}$ ,  $W_{Si} = 50 \mu\text{m}$ ,  $W_{NOA} = 26 \mu\text{m}$ .

**Figure S10:** Schematic illustration of bending geometries used for electrical characterization of mechanically flexible  $\mu$ -cell module.

**Figure S11:** Analytically calculated bending strain ( $\varepsilon_{yy}$ ) at the top (blue line) and bottom (red line) surface of silicon  $\mu$ -cell bent along the cell length direction as a function of the top polymer layer thickness ( $b$ ) in two different cases of with (dashed line) and without (continuous line) metal layer, where  $E_{Si} = 150$  GPa,  $E_{NOA} = 1$  GPa,  $E_{Au} = 78$  GPa,  $a = 30$   $\mu\text{m}$ ,  $t = 15$   $\mu\text{m}$ ,  $t_m = 0.6$   $\mu\text{m}$ ,  $W_{Si} = 50$   $\mu\text{m}$ ,  $W_{NOA} = 26$   $\mu\text{m}$ ,  $R = 4.9$  mm.

**Figure S12:** Color contour plot of calculated bending strains ( $\varepsilon_{xx}$ ) through the cross-section of a mechanically flexible  $\mu$ -cell module, bent (a) outward and (b) inward along the cell width direction at  $R = 4.9$  mm, without metal layer.

**Figure S13:** Color contour plot of calculated bending strains ( $\varepsilon_{xx}$ ) through the cross-section of a mechanically flexible  $\mu$ -cell module, bent (a) outward and (b) inward along the cell width direction at  $R = 4.9$  mm, with metal layer.

**Figure S14:** Optical image of automated printing machine.

**Figure S15:** Schematic illustration of illumination geometry used for electrical characterization of mechanically flexible  $\mu$ -cell module. The center of the module composed of 68  $\mu$ -cells was aligned for normal incidence illumination, where the angle of incidence of light at the module edge is  $\sim 30^\circ$  for  $R = 4.9$  mm.

## **SUPPLEMENATRY TABLE**

### **TABLE LEGEND**

**Table S1:** Parameters used for simulating thickness dependence of Si solar cell efficiency using PC-1D<sup>®</sup> software package.

## **SUPPLEMENATRY MOVIE**

### **MOVIE LEGEND**

**Movie S1:** A movie presenting transfer printing process of silicon  $\mu$ -cells using automated printer (Figure S14).

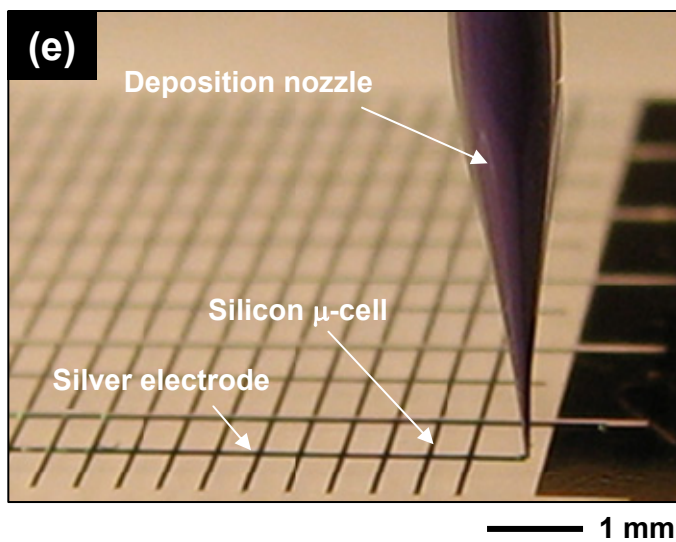
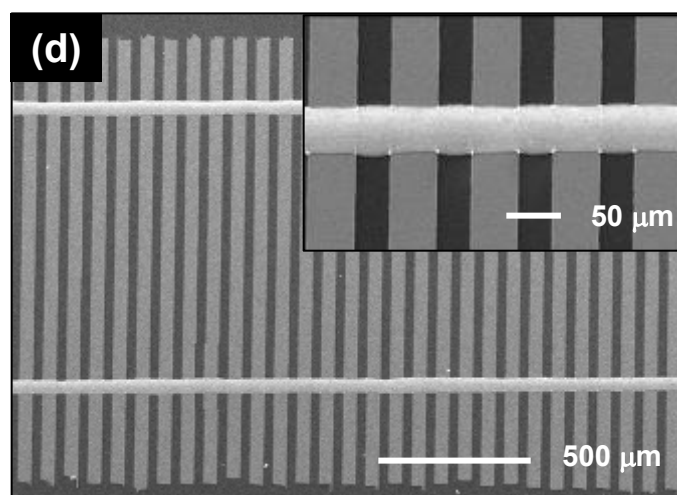
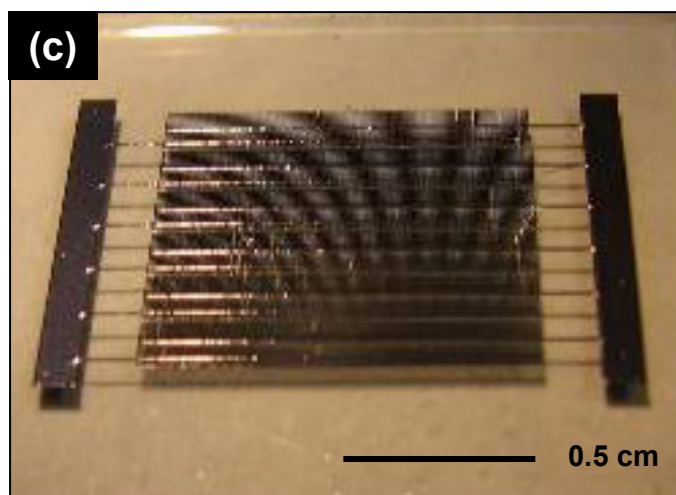
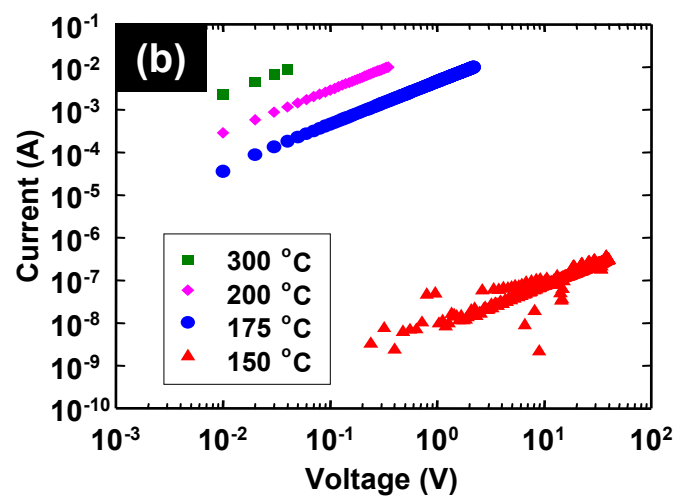
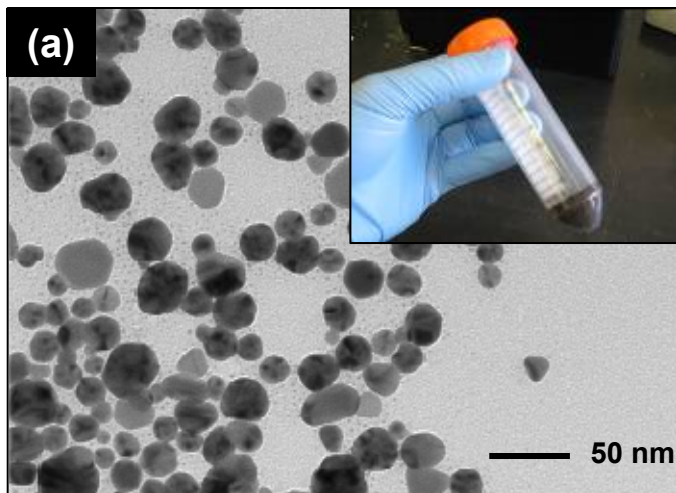


Figure S1.

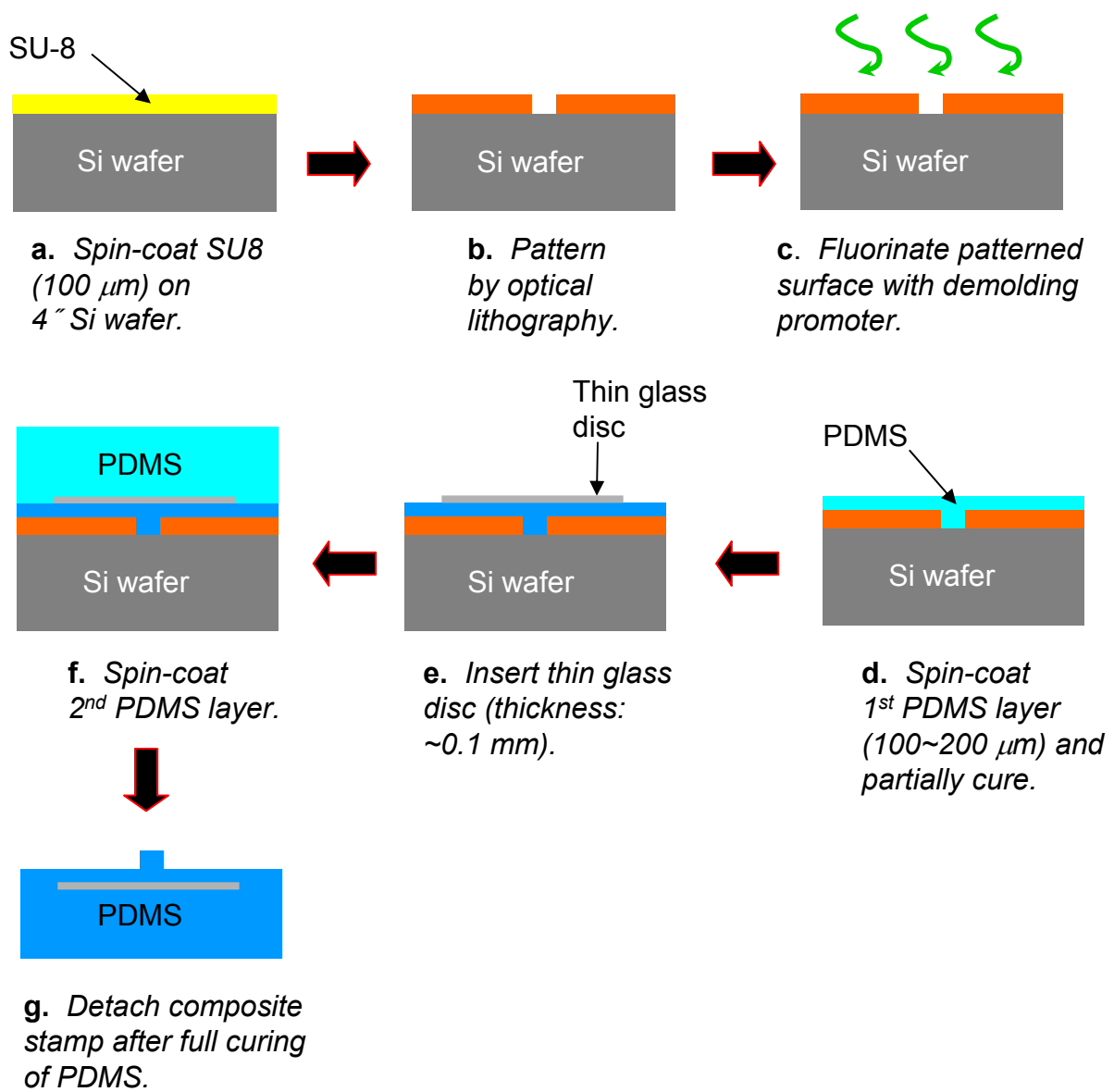


Figure S2.

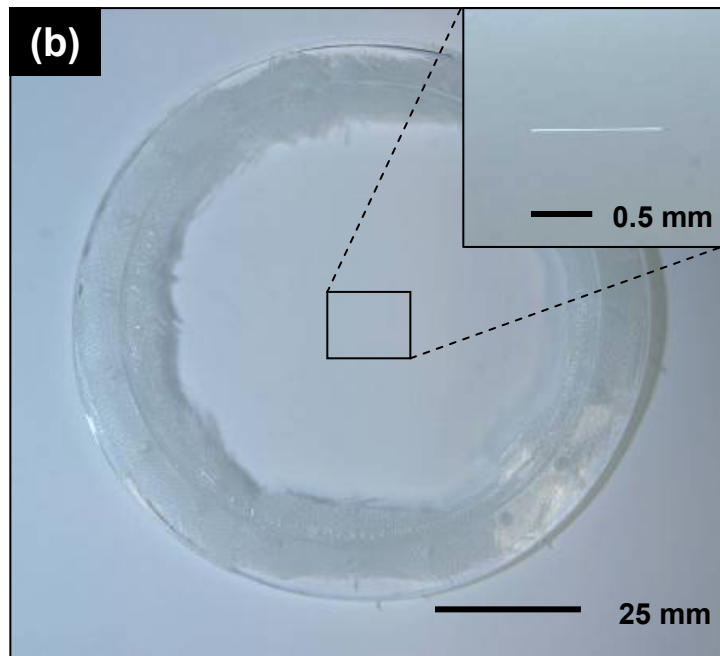
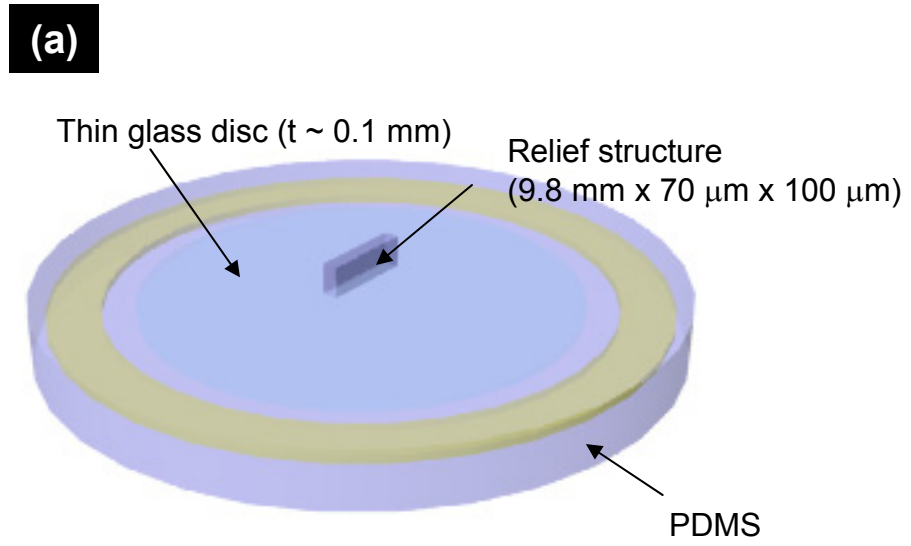
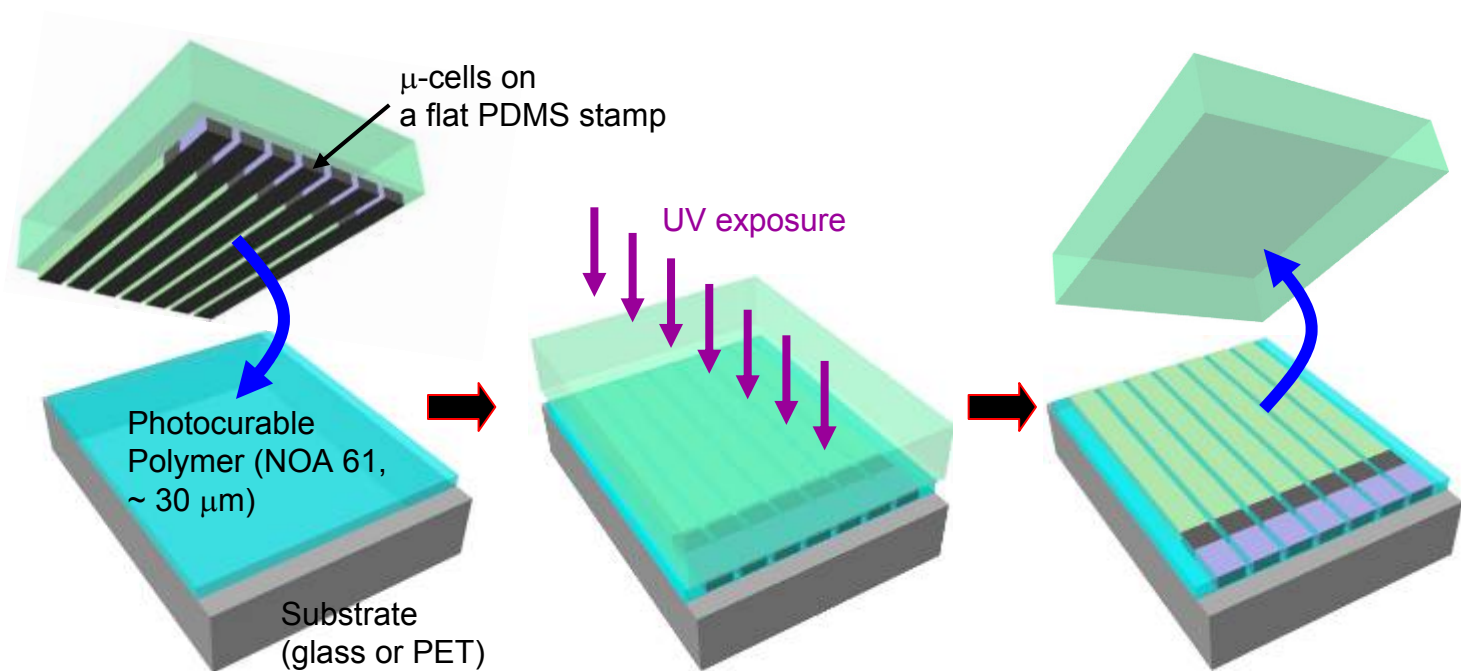


Figure S3.

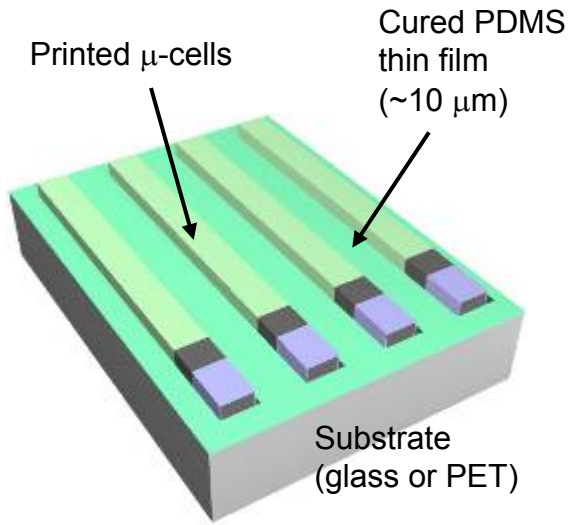


**a.** Print onto substrate coated with photocurable polymer.

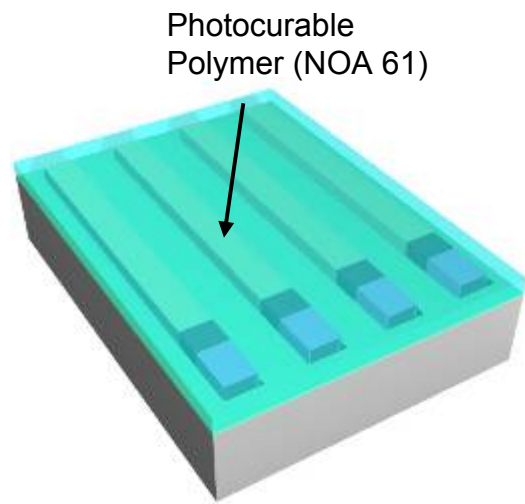
**b.** Cure under ultraviolet (UV) exposure.

**c.** Retrieve stamp after full curing, resulting in planarized  $\mu$ -cell arrays on receiving substrate.

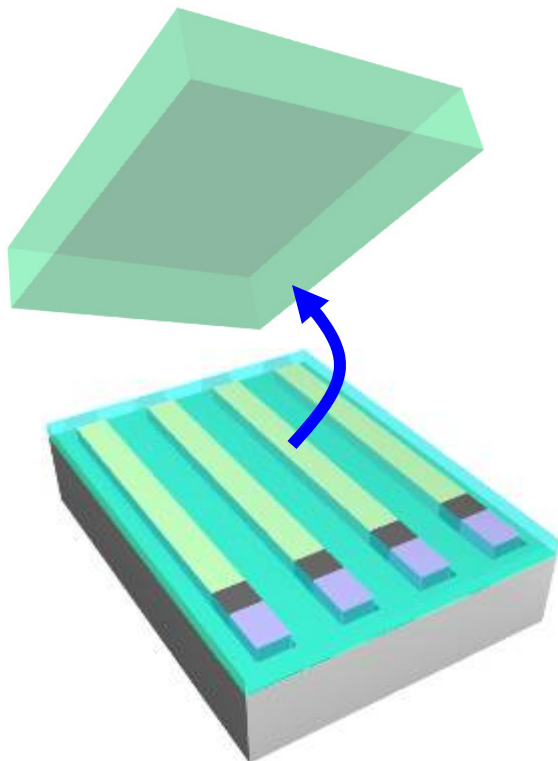
Figure S4.



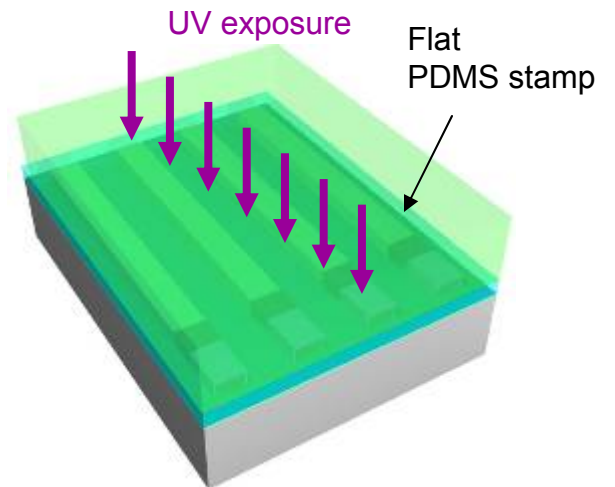
**a.** *Print onto thin PDMS coated substrate and evaporate SiO<sub>2</sub> (150 nm).*



**b.** *Spin-coat photocurable Polymer (~30 μm).*



**d.** *Retrieve stamp after full curing, followed by O<sub>2</sub> RIE to remove polymer residues on the cell surface.*



**c.** *Cure under UV exposure while a flat PDMS stamp is pressed above the spin-coated polymer layer.*



Figure S5.

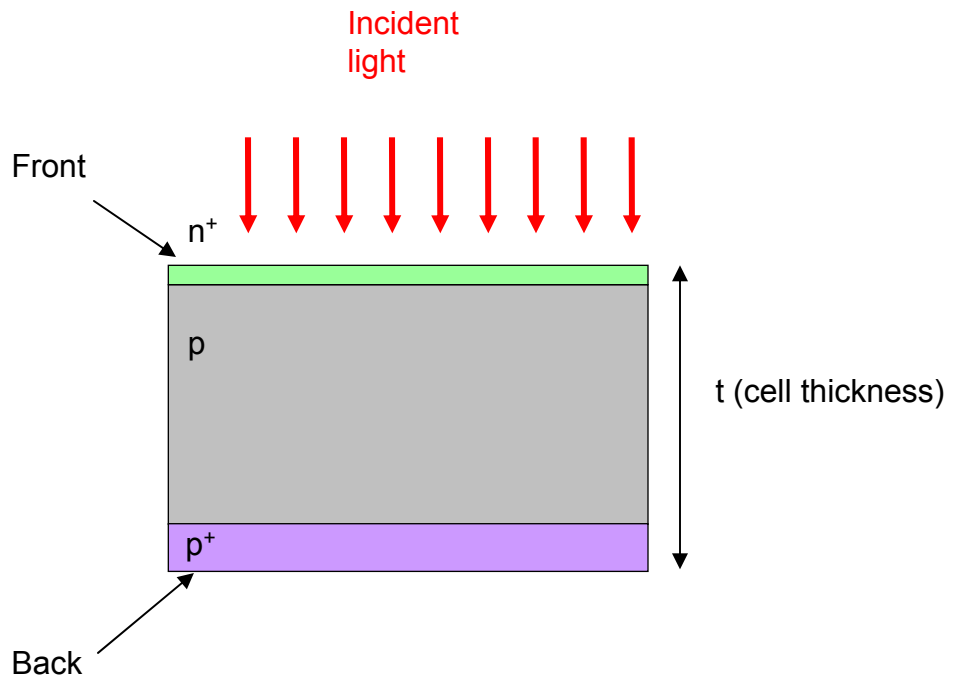


Figure S6.

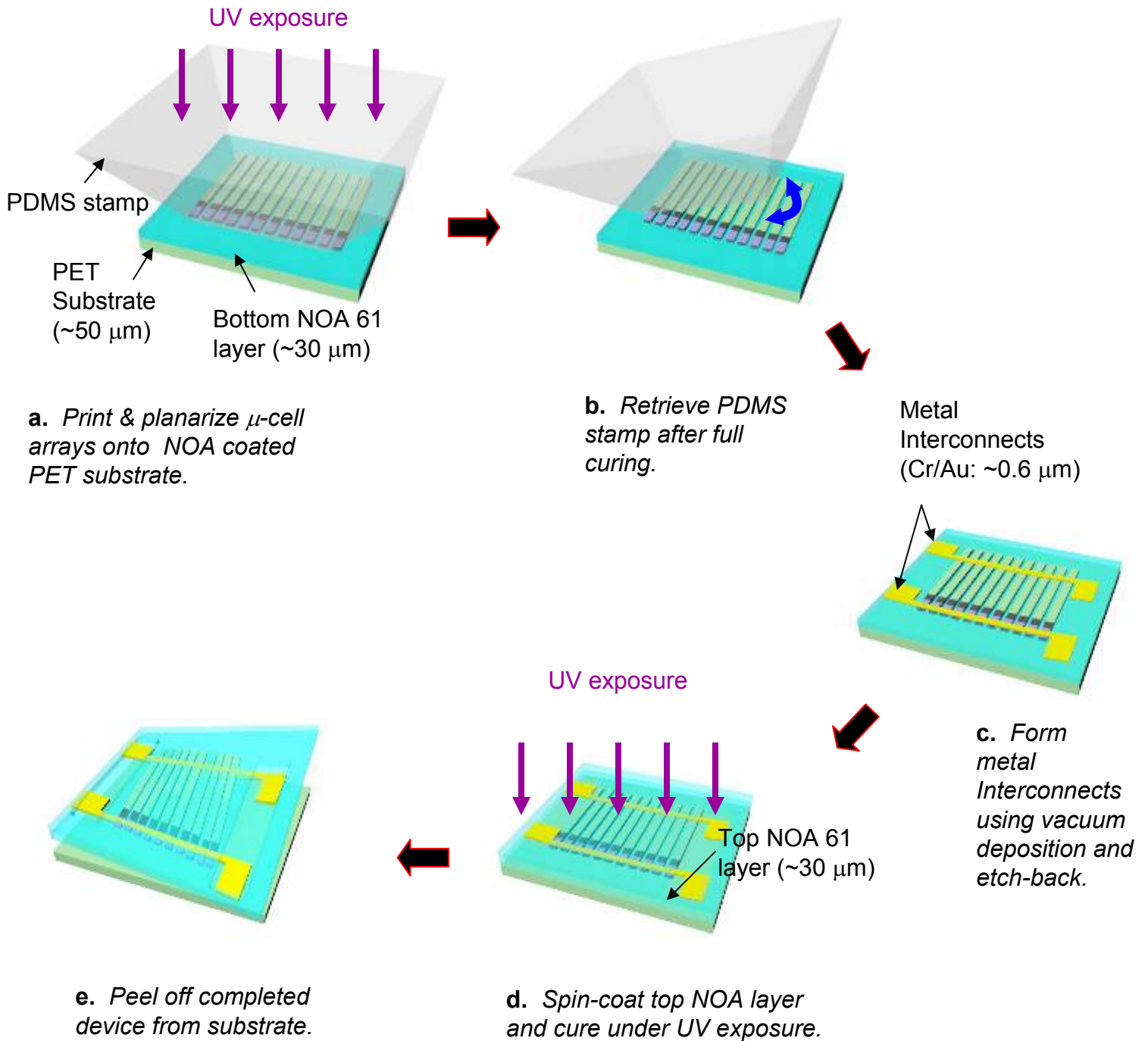
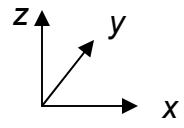
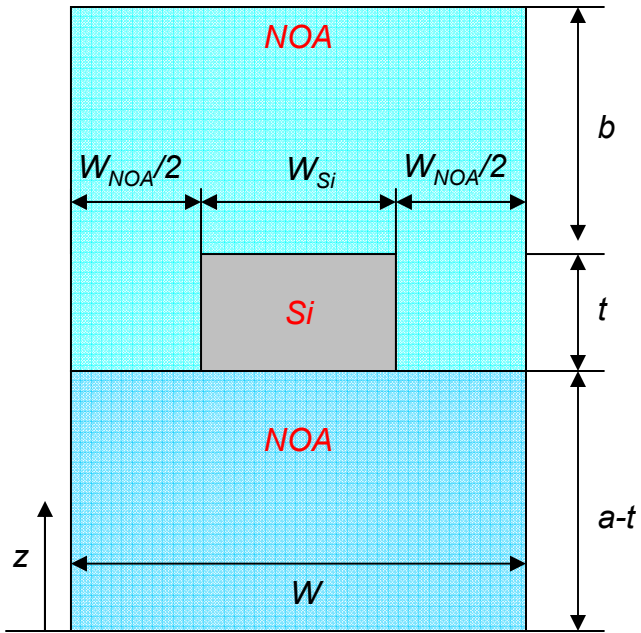


Figure S7.

(a)



(b)

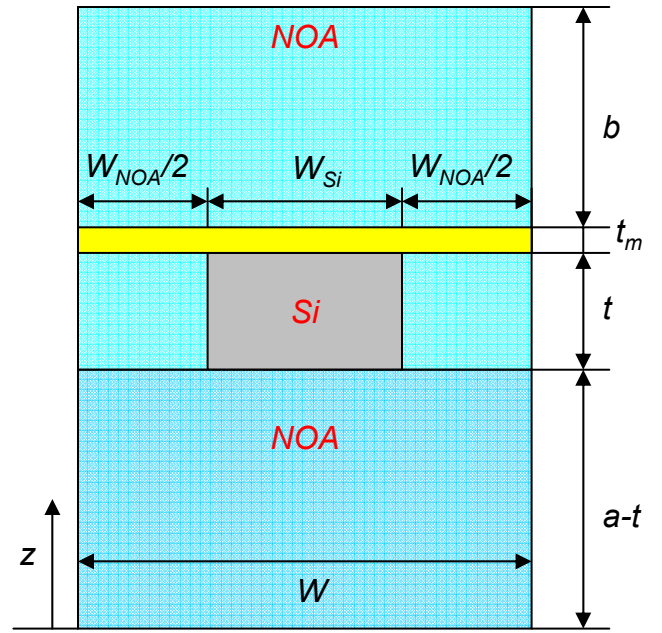


Figure S8.

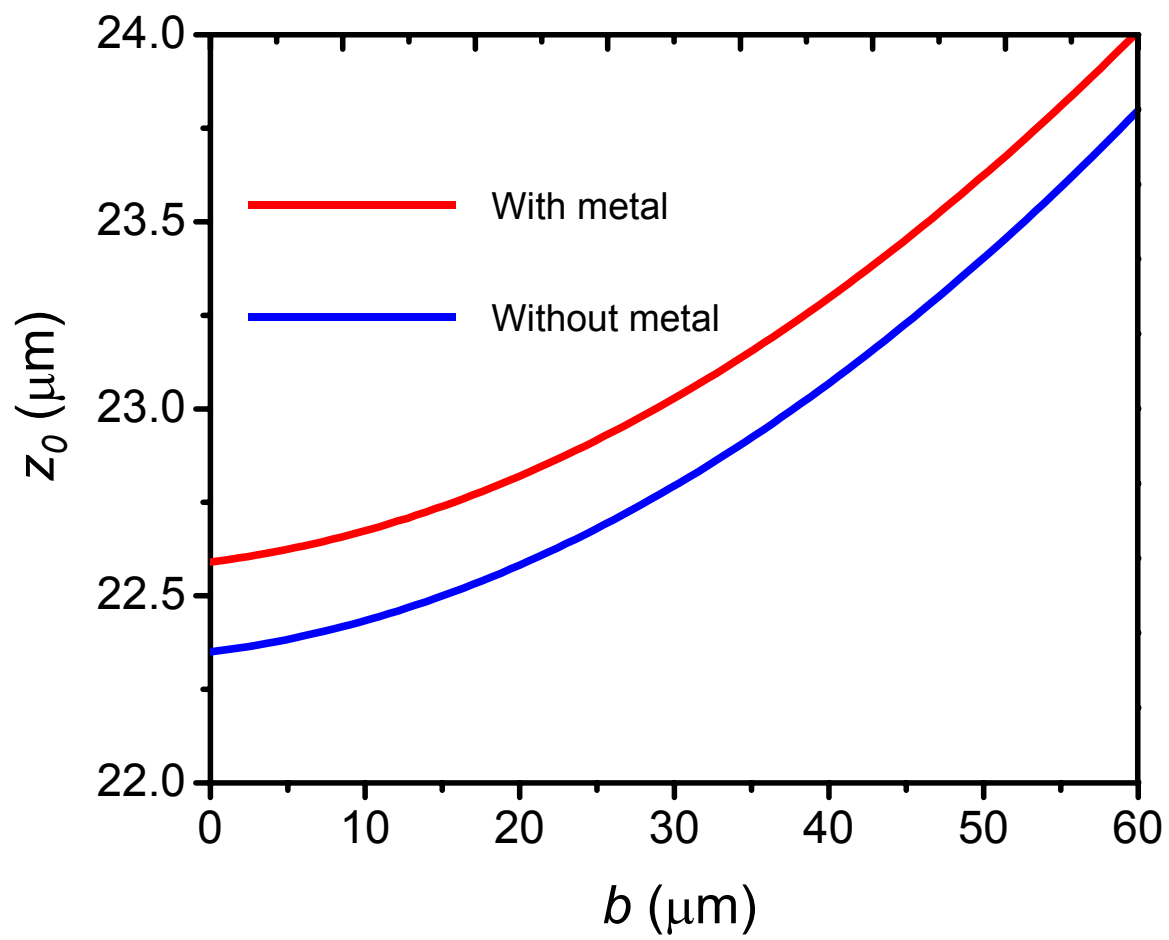


Figure S9.

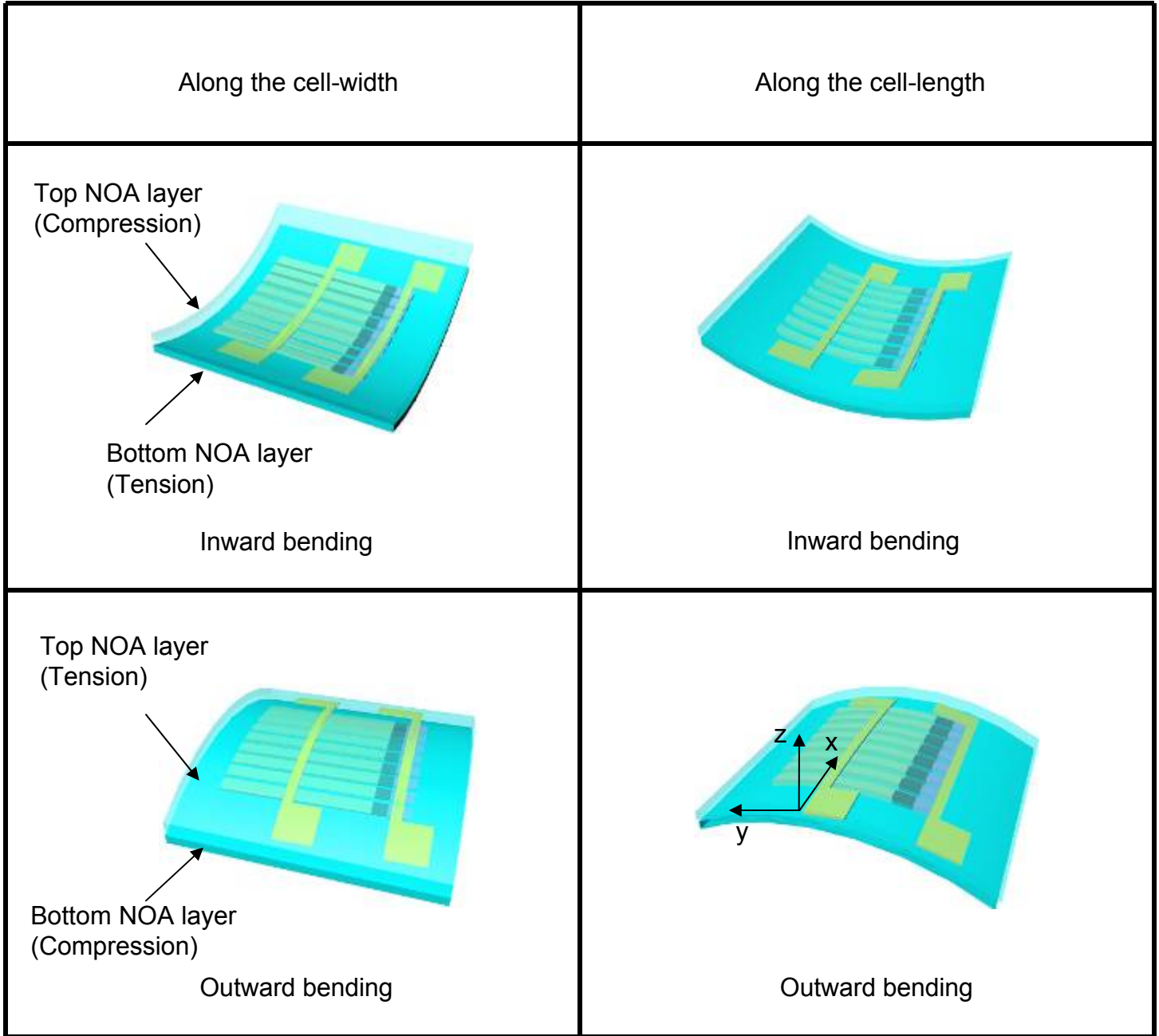


Figure S10.

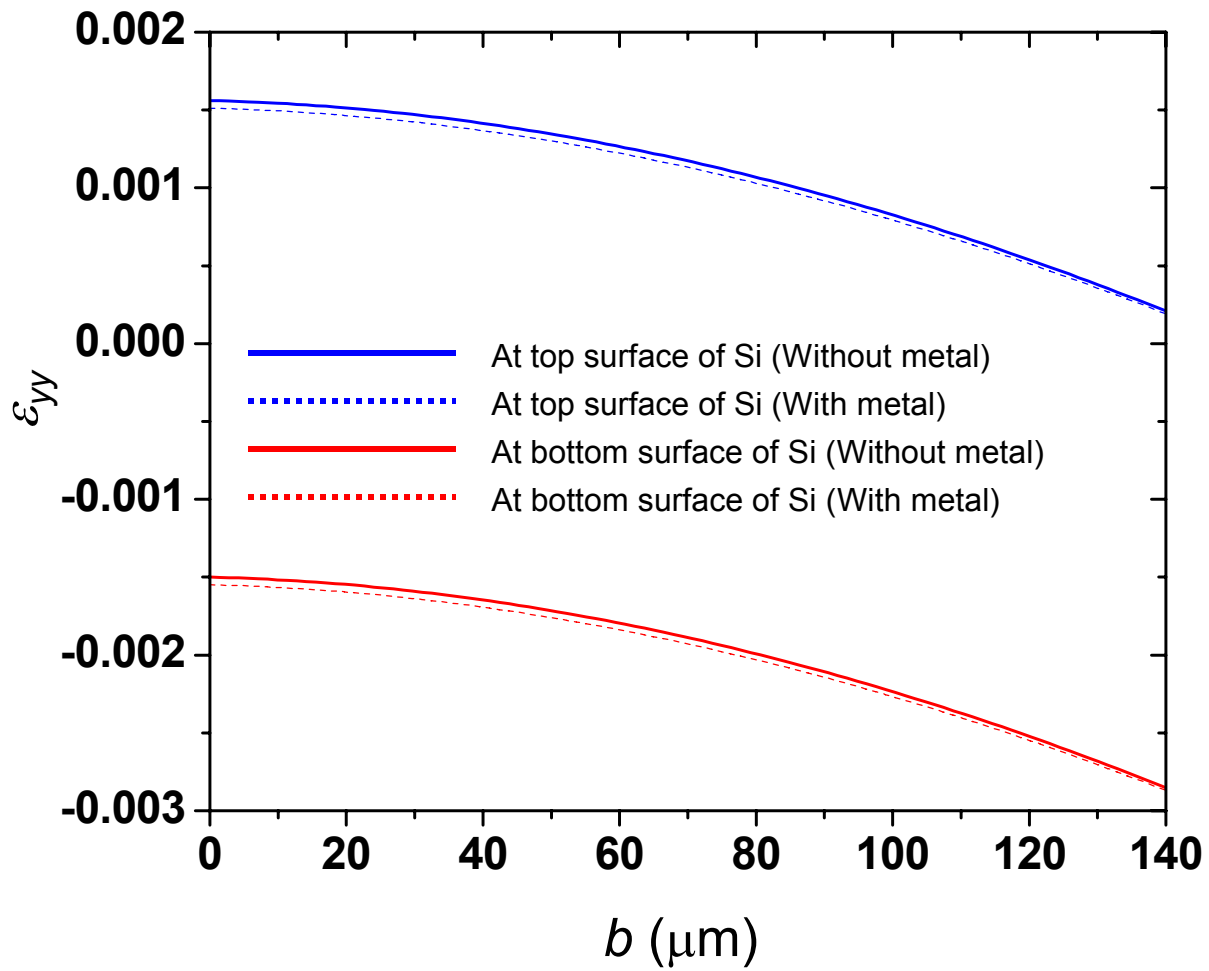
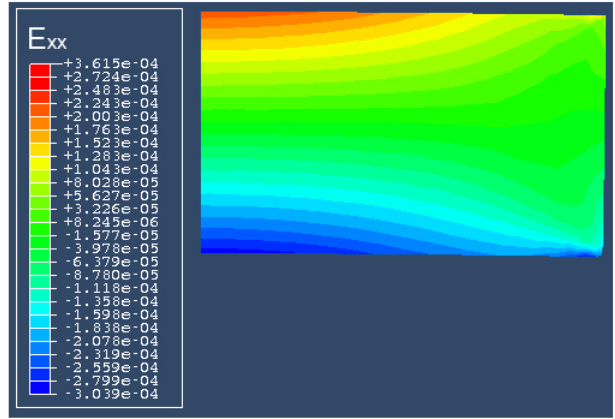
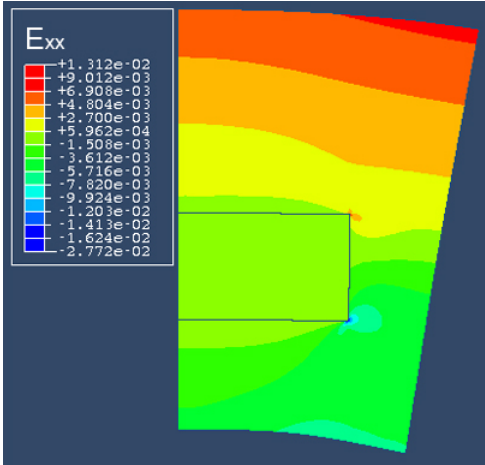


Figure S11.

(a)



(b)

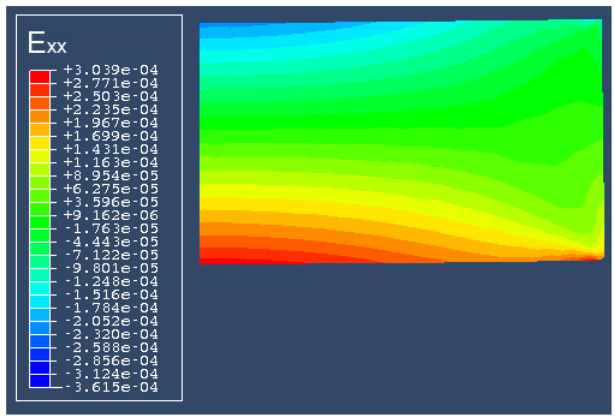
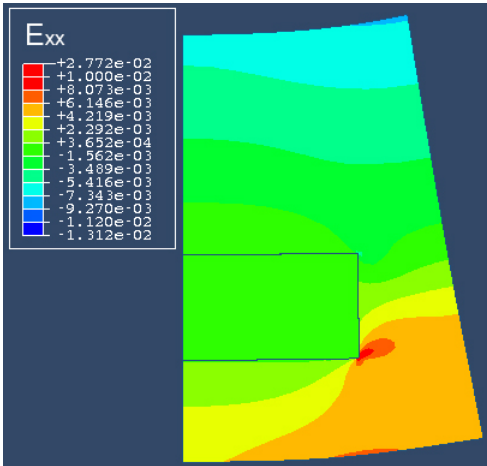
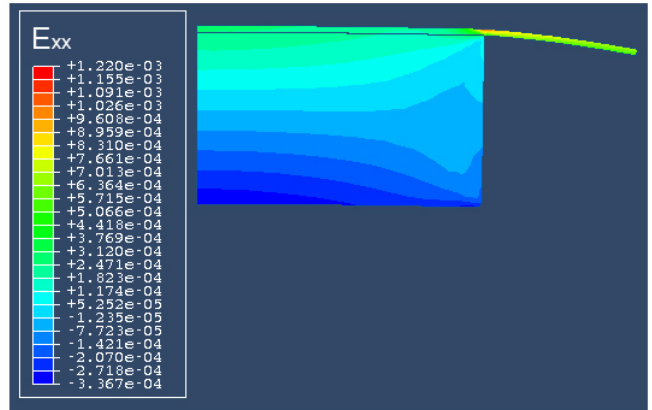
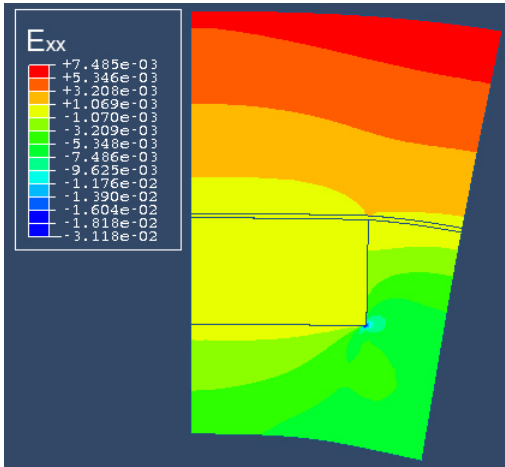


Figure S12.

(a)



(b)

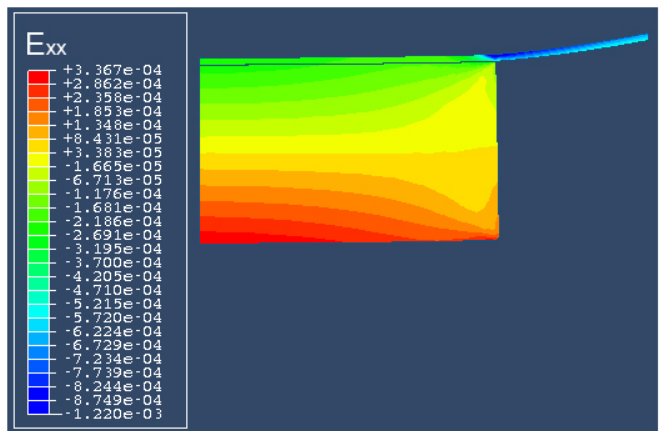
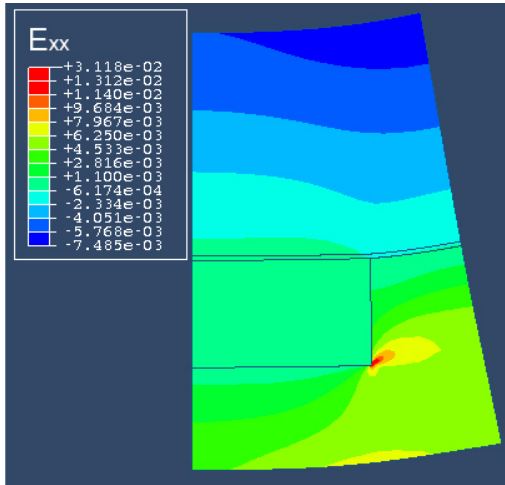
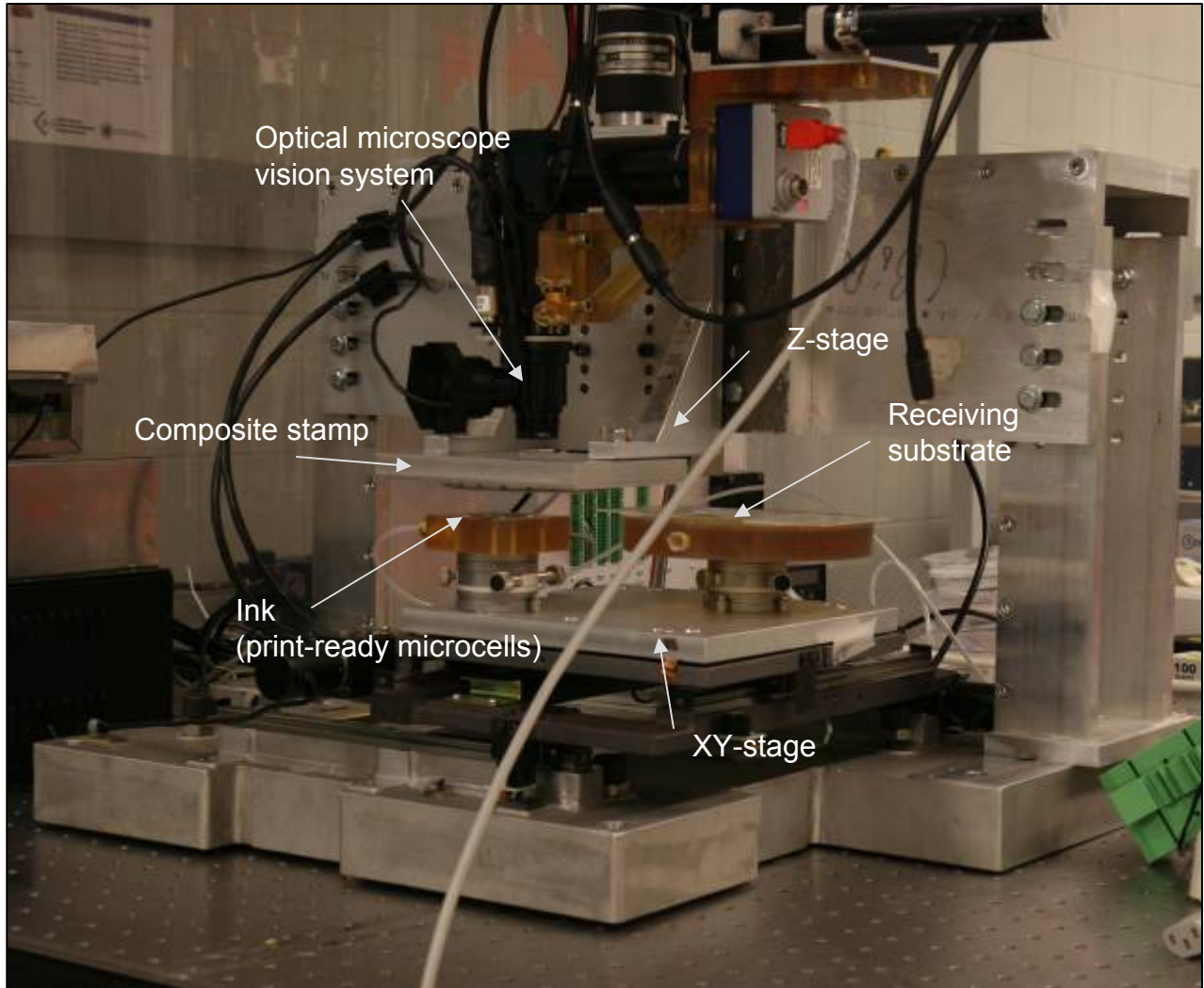
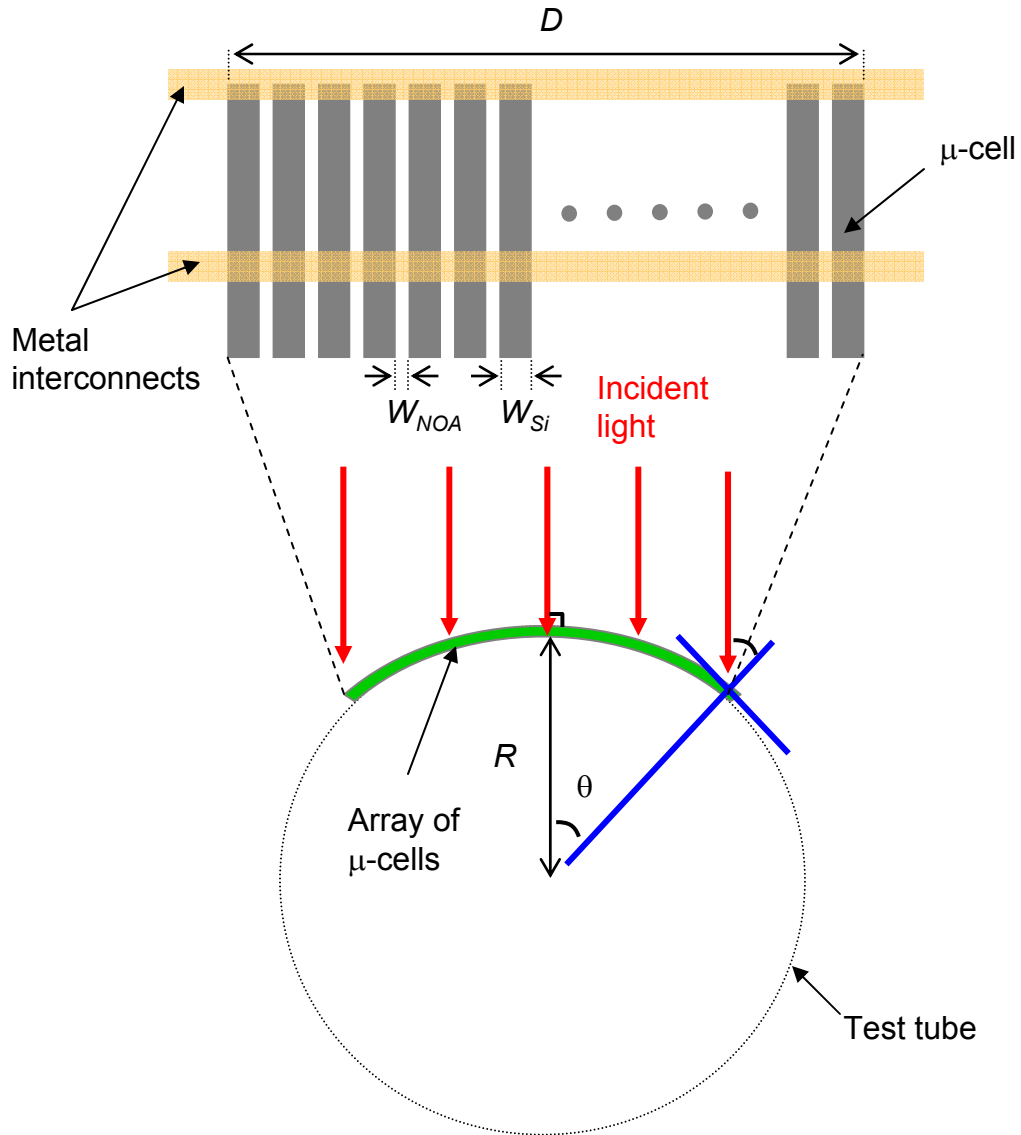


Figure S13.



10 cm

Figure S14.



$$D = (W_{Si} + W_{NOA}) \times (\# \text{ of cells}) - W_{NOA}$$

$W_{Si}$ : width of  $\mu$ -cell =  $50 \mu\text{m}$ .

$W_{NOA}$ : distance between adjacent  $\mu$ -cells =  $26 \mu\text{m}$ .

$D$ : total length of the array composed of 68 cells =  $5.142 \text{ mm}$ .

$$\theta = (1/2D)/R$$

$\theta$ : incidence angle of light at the edge of an array  $\sim 30^\circ$   
when  $R = 4.9 \text{ mm}$  and  $\# \text{ of cells} = 68$ .

Figure S15.

<b>Background materials (p)</b>	P-type boron doped Si (resistivity : 30 $\Omega$ .cm)
<b>Emitter doping (n<sup>+</sup>)</b>	Phosphorous, $4 \times 10^{20}$ cm <sup>-3</sup> , 0.25 $\mu$ m
<b>Base doping (p<sup>+</sup>)</b>	Boron , $1.8 \times 10^{20}$ cm <sup>-3</sup> , 1.8 $\mu$ m
<b>Bulk recombination life time</b>	7.208 ms for both electrons and holes
<b>Front/back surface recombination velocity</b>	$10^6$ cm/s for both electrons and holes
<b>Emitter contact resistance</b>	$10^{-6}$ $\Omega$
<b>Base contact resistance</b>	0.015 $\Omega$
<b>Exterior reflectivity</b>	5% (with antireflection coating and surface texturization), no back-side reflector.
<b>Temperature</b>	25°C
<b>Illumination</b>	AM1.5, 1000 W/m <sup>2</sup>

Table S1.